Quantum simulation of the spin-boson model with a microwave circuit

Juha Leppäkangas,[1,2] Jochen Braumüller,[2] Melanie Hauck,[1] Jan-Michael Reiner,[1] Iris Schwenk,[1] Sebastian Zanker,[1] Lukas Fritz,[1] Alexey V. Ustinov,[2,3] Martin Weides,[2,4] and Michael Marthaler[1,5,6]

[1]*Institut für Theoretische Festkörperphysik, Karlsruhe Institute of Technology, 76131 Karlsruhe, Germany*
[2]*Physikalisches Institut, Karlsruhe Institute of Technology, 76131 Karlsruhe, Germany*
[3]*Russian Quantum Center, National University of Science and Technology MISIS, 119049 Moscow, Russia*
[4]*Physikalisches Institut, Johannes Gutenberg University Mainz, 55128 Mainz, Germany*
[5]*Institut für Theorie der Kondensierten Materie, Karlsruhe Institute of Technology, 76131 Karlsruhe, Germany*
[6]*Theoretische Physik, Universität des Saarlandes, 66123 Saarbrücken, Germany*

(Received 7 February 2018; published 17 May 2018)

We consider superconducting circuits for the purpose of simulating the spin-boson model. The spin-boson model consists of a single two-level system coupled to bosonic modes. In most cases, the model is considered in a limit where the bosonic modes are sufficiently dense to form a continuous spectral bath. A very well known case is the Ohmic bath, where the density of states grows linearly with the frequency. In the limit of weak coupling or large temperature, this problem can be solved numerically. If the coupling is strong, the bosonic modes can become sufficiently excited to make a classical simulation impossible. Here we discuss how a quantum simulation of this problem can be performed by coupling a superconducting qubit to a set of microwave resonators. We demonstrate a possible implementation of a continuous spectral bath with individual bath resonators coupling strongly to the qubit. Applying a microwave drive scheme potentially allows us to access the strong-coupling regime of the spin-boson model. We discuss how the resulting spin relaxation dynamics with different initialization conditions can be probed by standard qubit-readout techniques from circuit quantum electrodynamics.

DOI: 10.1103/PhysRevA.97.052321

I. INTRODUCTION

The spin-boson model studies the dynamics of a two-level system interacting with a bosonic environment [1,2]. It is a generic model of quantum decoherence of two-level systems [3] and is of particular interest for the studies of quantum phase transitions [4]. It assumes a linear coupling between a two-level system (spin operator) and a collective coordinate of the bosonic bath. Despite its very simple form, the spin-boson model is not exactly solvable by any known theoretical method [2].

Certain limits of the spin-boson problem, however, are well understood. In the limit of weak system-bath coupling, perturbative methods such as the Born-Markov master equation [1,2] can be applied, describing weakly damped coherent oscillations. In the limit of high temperature, an adequate perturbation theory may be possible in the polaron basis [1,2,5], describing incoherent hopping of dressed states. In such situations, the corresponding spin-boson model can be solved in a good approximation, analytically or numerically. On the other hand, when interaction strengths are of the order of the involved frequencies, the problem becomes increasingly difficult, or even impossible, to solve in a desired accuracy. This regime covers many interesting problems of many-body physics, such as the Kondo effect [1,6,7] and localization-delocalization transitions of spin dynamics in different environments [1,4,8].

A commonly used strategy of obtaining new insight into many quantum models, or to test previous theoretical predictions, is the approach of quantum simulation [9–13]. The Hamiltonian of the problem is mapped to a well-controlled artificial quantum system and its dynamics is probed experimentally. Superconducting microwave circuits have proven to be a particularly attractive experimental platform for engineering various interesting Hamiltonians [14–21] due to their good controllability and feasibility of realizing exotic parameter regimes [22–26].

The computational complexity of model Hamiltonians is connected to the mutual coupling strengths of the individual elements relative to the subsystem energies. Reaching the strong-coupling regime between a qubit and a resonator in a superconducting microwave circuit, described by the Jaynes-Cummings model, has enabled the reproduction of many fundamental phenomena from cavity quantum electrodynamics (QED) and has led to the development of novel quantum systems and applications [22–25,27–29]. Here the coupling strength between the qubit and the bosonic mode is larger than the decay rates of the two coupled systems. If the coupling strength becomes comparable to the subsystem energies, the counterrotating terms of the general quantum Rabi model cannot be neglected. This ultrastrong-coupling regime [30–32] has been experimentally demonstrated with superconducting circuits [33–39] and in various other platforms [40–42]. Interesting phenomena that emerge include ground-state squeezing [43], single-mode phase transitions [44], and nonclassical state generation [45–47].

The spin-boson model is a generalization of the single-mode quantum Rabi model to a continuous-mode environment. Near the coupling regime that exhibits Kondo physics and localization-delocalization transitions [1,4,8], the energy decay rate Γ of the two-level system and its free-evolution frequency Δ are comparable, $\Gamma \lesssim \Delta$ [48,49]. A quantum

simulation of this region with superconducting microwave circuits can be done by connecting a superconducting qubit to an open transmission line [6,7,48,49]. Very strong couplings (combined with high qubit anharmonicities) are possible by designing system characteristic impedances comparable to the resistance quantum $R_Q = h/(2e)^2$ [6,7,48,49]. The single Cooper-pair charge $2e$ appears since the anharmonicity of the system is ultimately based on Cooper-pair tunneling across a Josephson junction. For the two-level approximation to hold even under strong dissipation, Cooper-pair tunneling must remain the dominant mechanism. In other words, the coupling strength must be lower than the qubit anharmonicity such that only very nonlinear qubits such as flux-based qubits are compatible with reaching the ultrastrong-coupling regime in the laboratory frame.

Besides increasing the coupling strength via sample design, it also can be effectively increased by creating a Hamiltonian in the rotating frame, based on the application of Rabi drives [18,50]. In the effective frame, the subsystem energies of the original problem are down-converted to lower frequencies, while the coupling strength is preserved up to a factor of 2. Applying this approach, an effective ultrastrong coupling between a microwave resonator and a superconducting qubit has recently been demonstrated also experimentally [20,51]. Here the original qubit-resonator system in the laboratory frame needs to be only in the strong-coupling regime. In this work we study an extension of this approach to a continuous-mode environment, yielding the spin-boson model. Recently, related approaches to effectively achieve ultrastrong coupling have been proposed based on parametric driving [52,53].

In this article we study theoretically a realization of the spin-boson model with strong system-environment couplings using a superconducting qubit coupled to an engineered environment of bosonic modes. In analogy to the approach described in Refs. [18,20], we propose the construction of an effective spin-boson Hamiltonian in the rotating frame. The bosonic environment is realized via a set of individual microwave resonators that reside in a restricted frequency range. We discuss in detail how the microwave circuit maps onto the spin-boson model discussed in literature. While in principle any bosonic environment can be engineered with the proposed method, we consider the construction of an environment with an Ohmic spectral function that allows for probing localization dynamics of the spin-boson model. We find that the localization regime appears at strong coupling between the qubit and individual bosonic modes, which is experimentally feasible to achieve.

We also discuss how the resulting spin dynamics can be probed by standard readout techniques from circuit QED. In particular, the down-conversion of system frequencies allows for tracking the spin-relaxation dynamics in real time. We also discuss an experimental implementation, where the bosonic environment and the qubit are fabricated on two separate chips in a modular approach. This setup allows for probing the system more rigorously, by characterizing both the qubit and the environmental properties in separate experiments.

The article is organized as follows. In Sec. II we introduce the spin-boson problem in the notation widely used in literature and how it maps to the notation and methods used in this article. We briefly go through central results and predictions of the spin-boson model. In particular, in Sec. II C we show how the effective spin-boson coupling strength can be tailored by two-tone driving. In Sec. III we introduce an implementation of the spin-boson model by a superconducting transmon qubit coupled to a microwave circuit. We show how the impedance of the environment is related to the spectral density in the spin-boson model and discuss in detail how the impedance affects to transmon. In Sec. IV we analyze how a set of microwave resonators can be used to tailor an Ohmic spectral density in the rotating frame with Kondo parameter $\alpha \sim 1$. In Sec. V we provide a description of an experimental realization based on a modular flip-chip approach and introduce measurement pulse sequences that can be used to probe spin dynamics with different initial conditions. A summary and discussion are given in Sec. VI.

II. SPIN-BOSON MODEL

We start our analysis by introducing the Hamiltonian and the spectral function of the spin-boson problem. After this, in Sec. II B, we go through central results and predictions of the spin-boson problem obtained in the literature [1] and discuss the corresponding quantities to be measured in our realization. In Sec. II C, by applying the method described in Refs. [18,20], we derive an effective spin-boson Hamiltonian in the rotating frame with decreased subsystem energies. Finally, in Sec. II D we analyze the limits of validity of the given derivation.

A. Spin-boson Hamiltonian and the spectral density

Here we introduce the spin-boson Hamiltonian in the notation widely used in earlier literature. After this we discuss how it maps to the notation used in this article. The notation and methods used throughout the remainder of this article match the standard ones used in superconducting microwave circuits and therefore more directly allow us to relate properties of the spin-boson model to the proposed experimental realization.

1. Notation in literature

In earlier literature, the spin-boson model is often introduced by starting from the Hamiltonian [1,2]

$$\hat{H}_{\rm SB} = -\frac{\hbar\Delta}{2}\hat{\sigma}_x + \frac{\epsilon}{2}\hat{\sigma}_z + \frac{q_0}{2}\hat{\sigma}_z\sum_i c_i\hat{x}_i + \hat{H}_{\rm bath}, \quad (1)$$

$$\hat{H}_{\rm bath} = \sum_i\left[\frac{1}{2}m_i\omega_i^2\hat{x}_i^2 + \frac{1}{2m_i}\hat{p}_i^2\right]. \quad (2)$$

The two-level system, described by the Pauli matrices $\hat{\sigma}_i$, may be regarded as two trapped positions of a virtual particle in a certain potential landscape. The variable q_0 denotes a trapping distance, Δ denotes a hopping rate, and ϵ characterizes the energy difference. The environment perceives the location of the particle and thereby couples to $\hat{\sigma}_z$. The free evolution of the environmental coordinate operators $\hat{x}_i$ is defined by the quadratic harmonic oscillator Hamiltonian $\hat{H}_{\rm bath}$.

A central function of the theory is the spectral density of the environment, defined formally as

$$J(\omega) = \frac{\pi}{2}\sum_i\frac{c_i^2}{m_i\omega_i}\delta(\omega-\omega_i). \quad (3)$$

The spectral function $S(\omega)$ of the collective bath operator,

$$\hat{X} = \sum_i c_i \hat{x}, \tag{4}$$

is a function of temperature T and $J(\omega)$ and reads

$$S(\omega) = \langle \hat{X}(t)\hat{X}(0)\rangle_\omega = \frac{2\hbar J(\omega)}{1-\exp\left(-\frac{\hbar\omega}{k_B T}\right)}. \tag{5}$$

Together with the parameter q_0 [see Eq. (1)], the spectral function includes all relevant information of the effect of the environment on the two-level system. The fundamental reason is that the environmental fluctuations satisfy Gaussian statistics. Accordingly, Wick's theorem is valid and the time evolution of the reduced density matrix of the two-level system is fully described by two-time correlation functions of the environmental coupling operator.

2. Notation in this article

When superconducting qubits are capacitively or inductively coupled to microwave cavities, their dipole moment couples to the electric or magnetic field of the cavity. Since the dipole coupling is considered transversal, it is intuitive to write the coupling term proportional to a $\hat{\sigma}_x$ operator. Therefore, even though circuit QED systems consisting of a superconducting qubit coupled to a set of microwave resonators are described by the spin-boson Hamiltonian in Eq. (1), their Hamiltonian is usually written down in a notation where the definitions of $\hat{\sigma}_x$ and $\hat{\sigma}_z$ are interchanged, most typically in the context of the Jaynes-Cummings model [28]. In the case of a transmon qubit [54], the two energy levels correspond to two eigenstates of a virtual particle in the same potential minimum.

To keep the notation comparable with Sec. II A 1, we define the system parameters analogously to the above. We then consider establishing the spin-boson Hamiltonian using a superconducting qubit with energy splitting $\hbar\Delta$, coupled to a set of microwave resonators, described by the total Hamiltonian

$$\hat{H} = \frac{\hbar\Delta}{2}\hat{\sigma}_z + \frac{q_0}{2}\hat{\sigma}_x \sum_i g_i(\hat{b}_i + \hat{b}_i^\dagger) + \sum_i \hbar\omega_i \hat{b}_i^\dagger \hat{b}_i. \tag{6}$$

This corresponds to the case $\epsilon = 0$, which is the regime that shows the physically most relevant and nontrivial behavior [1]. This Hamiltonian is well implemented by a quantum circuit based on the transmon qubit [54]. The spectral density, defined in Eq. (3), becomes

$$J(\omega) = \frac{\pi}{\hbar}\sum_i g_i^2 \delta(\omega - \omega_i). \tag{7}$$

We note that the coupling parameter q_0 could also be incorporated in the definition of the coupling strengths g_i. Our separation is meaningful only when the variables $c_i\hat{x}_i = g_i(\hat{b}_i + \hat{b}_i^\dagger)$ correspond to certain physical quantities. In this article we fix the bath coordinates $\hat{x}_i$ to correspond to voltage fluctuations across the two capacitors of the qubit,

$$\hat{X}(t) \equiv \hat{V}(t). \tag{8}$$

Therefore, q_0 has the dimension of charge. It describes an effective charge shift of the artificial atom between its two states as seen by the environment. The variable q_0 then absorbs all the information of the qubit and how it couples to the voltage fluctuations: The following results are thereby valid, in principle, for arbitrary superconducting qubits with appropriate adaptations of coupling parameter q_0. Within this identification we then write

$$\langle \hat{V}(t)\hat{V}(0)\rangle_\omega = \frac{2\hbar J(\omega)}{1-\exp\left(-\frac{\hbar\omega}{k_B T}\right)}, \tag{9}$$

following from Eq. (5) and the identification made in Eq. (8).

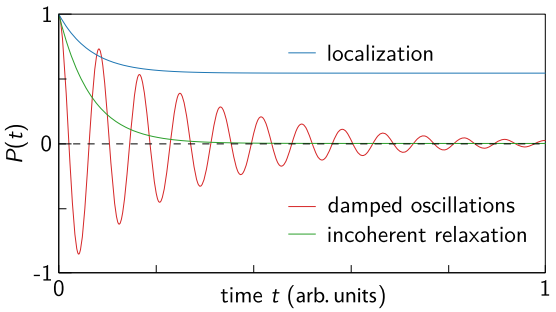

FIG. 1. Qualitative behavior of spin dynamics in the three main regimes of the spin-boson model with an Ohmic environment ($s = 1$). The probability $P(t)$ corresponds in the proposed system to the expectation value $P(t) = \langle\hat{\sigma}_x(t)\rangle$, when initialized to the $+1$ eigenstate of σ_x at $t = 0$. For $\alpha < 0.5$, (damped) oscillations prevail when $\hbar\Delta_{\rm rn} \gtrsim \alpha k_B T$, but change to incoherent relaxation when $\hbar\Delta_{\rm rn} \lesssim \alpha k_B T$ (exponential decay to zero). Localization effect leads to a decay of $P(t)$ towards a finite value and occurs for $\alpha \geqslant 1$ and $T = 0$. In other regimes, the system exhibits incoherent relaxation with subtle forms of the decay rate [1].

B. Different bath spectral functions and predictions for the relaxation dynamics of the spin-boson model

In the following, we briefly go through some central predictions made for the spin dynamics when interacting with bosonic environments of different spectral functions. We explain how these predictions correspond to the dynamics in the considered circuit QED system. A more detailed explanation of an experimental realization is given in Sec. V. Central predictions for an Ohmic environment are summarized qualitatively in Fig. 1.

1. Measured quantities

In the spin-boson model, a widely studied effect is the hopping dynamics between the two trapped positions of the fictitious particle (connected by the hopping amplitude Δ) under a perturbation caused by coupling to the environment. Here we are not interested in the environment itself, but in the short- and intermediate-timescale evolution of the system when subjected to a certain initial condition. The long-time behavior is also interesting to study, but can be much more challenging to observe in experiment. The theoretical restrictions to short and intermediate timescales practically correspond to the experimental restrictions due to the finite initialization time and finite decoherence time of the superconducting qubit, correspondingly.

We consider now the notation introduced in Sec. II A 2 and follow the discussion given in Ref. [1]. If inserted initially in the left-hand side well, the probability of the particle to be

found from this well again at some later time depends on the hopping amplitude and interaction with the environment. (For a rigorous mathematical definition of the problem, particularly the initialization of the system, see Ref. [1].) Such population dynamics corresponds in our notation to the initialization of the system at $t = 0$ to an eigenstate of operator $\hat{\sigma}_x$ and measuring the value of $\hat{\sigma}_x$ at certain later time $t > 0$,

$$P(t) = \langle \hat{\sigma}_x(t) \rangle. \tag{10}$$

Ideally, in the absence of interaction, we get (defining the left-hand side as the $+1$ eigenstate of $\hat{\sigma}_x$)

$$P(t) = \cos \Delta t. \tag{11}$$

When interacting with the environment, the hopping can become damped, overdamped, or even totally forbidden (localization).

We note that in our realization, we are naturally not restricted to the theoretical scenarios in the literature: One can probe both $\hat{\sigma}_z$ and $\hat{\sigma}_x$ with different initialization conditions for the two-level system as well as for the bath (see Sec. V). The exact initialization of the bath affects the results essentially in the case of strong couplings, while it is not a requirement for the observation of the following effects (in particular the localization).

2. *Relaxation dynamics for different environments*

A central example of the spin-boson model is the Ohmic environment, which is described by a linear spectral density

$$J(\omega) = \eta \omega F_c(\omega). \tag{12}$$

Here we have introduced a cutoff function $F_c(\omega)$. For instance, this can be an exponential drop $F_c(\omega) = e^{-\omega/\omega_c}$ or a sharp cutoff $F_c(\omega) = \Theta(\omega_c - \omega)$, with cutoff frequency ω_c. An important parameter describing the coupling between the system and the environment in the Ohmic case is the Kondo parameter

$$\alpha = \eta \frac{q_0^2}{2\pi\hbar}. \tag{13}$$

It can be qualitatively interpreted as an environment-induced decay rate Γ normalized by the internal precession frequency Δ, $\alpha \sim \Gamma/\Delta$. In the limit $\alpha \ll 1$, it directly corresponds to an inverse quality factor of the weakly perturbed two-level system, as derived in Sec. III D, and a similar result can also hold for the quantum two-level system with $\alpha \sim 1$ [48,49], even though here a separation between the system and environment dynamics is not necessary that clearly defined.

It has been understood that we have practically two independent variables that define the solution of the problem: the interaction strength α and the (bath renormalized) two-level system energy $\Delta_{\rm rn}$ [1]. Under the influence of the environment, many qualitatively different behaviors of the well-hopping dynamics can occur. For $\alpha < 1/2$ we can have damped oscillations ($\Delta_{\rm rn} \gtrsim k_B T\alpha$) changing to incoherent relaxation ($\Delta_{\rm rn} \lesssim k_B T\alpha$). For $\alpha > 1/2$, all dynamics are expected to be incoherent. In the regime $\alpha \geqslant 1$ and $T = 0$, one expects a total suppression of hopping, whereas for $T \gtrsim 0$ very slow thermal relaxation should occur [1]. In the simple Ohmic case with a linear increase of $J(\omega)$, we therefore expect very different types of behavior in various parameter regimes. The regimes are summarized in Fig. 1.

It can be helpful to mention that the localization mechanism in the spin-boson model is closely related to the Coulomb blockade effect in superconducting tunnel junctions, i.e., Cooper-pair tunneling across a Josephson junction that is voltage biased in series with an electromagnetic environment. When the environmental (zero-frequency or characteristic resonator) impedance is comparable to the resistance quantum $R_Q = h/4e^2$, the system enters the Coulomb blockade regime, where charge tunneling is strongly suppressed or even completely prohibited [55–58].

The model for the general power-law behavior of $J(\omega)$ is conveniently written in the form

$$J(\omega) = A_s \omega^s \omega_c^{1-s} F_c(\omega). \tag{14}$$

Here the case $s < 1$ is called the sub-Ohmic regime and $s > 1$ is referred to as the super-Ohmic regime. In particular, $s = 0$ with $T > 0$ has been used as a model for $1/f$ noise [3,5]. The super-Ohmic case appears in the electron tunneling in solids with coupling to a (three-dimensional) phononic bath. The extra scaling factor ω_c^{1-s} has been introduced so that we can define a dimensionless variable $\mathcal{A} = A_s q_0^2/2\pi\hbar$, in analogy to the Kondo parameter α. However, it has less physical meaning here than in the Ohmic case. It also always appears together with the scaling introduced by the cutoff $\mathcal{A}\omega_c^{1-s}$ [1]. In a rough overall picture, the super-Ohmic case shows mostly damped oscillations and does not exhibit localization, whereas the sub-Ohmic case is less trivial; it is localized for weak tunneling amplitudes Δ (depending on $\mathcal{A}$) but even there, in nonequilibrium, can show coherent oscillations [8]. Also as opposed to the Ohmic case, here more than one relevant energy scale of coherent dynamics exists.

C. Simulation in the rotating frame

Here we show how to establish an effective spin-boson Hamiltonian in the rotating frame by additional microwave driving. We take use of modified interaction during driven evolution of the two-level system [59]. An important detail of the following derivation is that even though rotating-wave approximations (RWAs) can be taken in various places of the derivation, one cannot be taken for the final effective Hamiltonian, where the effect of counterrotating terms can be essential.

1. *Two-tone driving*

Following Refs. [18,20], we consider driving this system with two Rabi tones, both with transverse coupling to the qubit. A Hamiltonian that describes such a driven system has the form

$$\hat{H} + \hat{H}_d, \tag{15}$$

where the drive is accounted for by the term

$$\hat{H}_d = \hbar\Omega_1 \hat{\sigma}_x \cos\omega_1 t + \hbar\Omega_2 \hat{\sigma}_x \cos\omega_2 t. \tag{16}$$

Here Ω_i is the amplitude and ω_i the frequency of the drive i. To obtain an immediate feeling of the drive frequencies and amplitudes we use, we note that in the following scheme we consider a situation where $\omega_1 \gtrsim \omega_2$ and $\Omega_1 \gg \Omega_2$. During the derivation, also the condition $\omega_1 - \omega_2 = \Omega_1$ is taken to obtain

the desired form of the Hamiltonian (see below) and we will have $\omega_i \gg \Omega_i$. The drive frequency can be assumed to be the qubit frequency in the laboratory frame $\omega_1 = \Delta$.

We enter now a rotating frame with respect to the stronger transverse drive by performing a unitary transformation according to

$$\hat{U} = \exp\left[i\omega_1 t\left(\sum_i \hat{b}_i^\dagger \hat{b}_i + \frac{1}{2}\hat{\sigma}_z\right)\right]. \tag{17}$$

This is a combined rotating frame of the two-level system and of all the bosonic modes. The Hamiltonian becomes now

$$\begin{aligned}\frac{\hat{H}_1}{\hbar} &= \frac{1}{\hbar}(\hat{U}\hat{H}\hat{U}^\dagger - i\hat{U}\dot{\hat{U}}^\dagger) = \frac{\Delta-\omega_1}{2}\hat{\sigma}_z + \frac{\Omega_1}{2}\hat{\sigma}_x \\ &+ \sum_i(\omega_i-\omega_1)\hat{b}_i^\dagger\hat{b}_i + \frac{q_0}{2\hbar}\sum_i g_i(\hat{b}_i\hat{\sigma}_+ + \hat{b}_i^\dagger\hat{\sigma}_-) \\ &+ \frac{\Omega_2}{2}(e^{i(\omega_1-\omega_2)t}\hat{\sigma}_+ + e^{-i(\omega_1-\omega_2)t}\hat{\sigma}_-).\end{aligned} \tag{18}$$

We have neglected the contributions

$$\begin{aligned}\hat{O}_1 &= \frac{q_0}{2\hbar}\sum_i g_i\hat{\sigma}_+\hat{b}_i^\dagger e^{2i\omega_1 t} + \frac{\Omega_1}{2}\hat{\sigma}_+ e^{2i\omega_1 t} \\ &+ \frac{\Omega_2}{2}\hat{\sigma}_+ e^{i(\omega_1+\omega_2)t} + \text{H.c.}\end{aligned} \tag{19}$$

This can be done if oscillations with the frequencies $2\omega_1$ and $\omega_1+\omega_2$ are much faster than frequencies Ω_1 and Ω_2. In addition, coupling to modes in the bosonic bath, with couplings $q_0 g_i/\hbar$, is negligible if the bath will include only modes in a small frequency range $\omega_c \ll 2\omega_i$.

In the Hamiltonian of Eq. (18), the dominant term will be the contribution proportional to Ω_1. It is then favorable to move to the interaction picture defined by this term. This means performing another unitary transformation, this time according to

$$\hat{U} = \exp\left[i\frac{\Omega_1}{2}\hat{\sigma}_x t\right]. \tag{20}$$

We also choose $\Omega_1 = \omega_1 - \omega_2$, which leads to

$$\begin{aligned}\frac{\hat{H}_2}{\hbar} &= \frac{\Omega_2}{4}\hat{\sigma}_z + \frac{q_0}{2\hbar}\sum_i \frac{g_i}{2}\hat{\sigma}_x(\hat{b}_i^\dagger + \hat{b}_i) \\ &+ \sum_i(\omega_i-\omega_1)\hat{b}_i^\dagger\hat{b}_i.\end{aligned} \tag{21}$$

We have again neglected fast oscillating terms

$$\begin{aligned}\hat{O}_2 &= \frac{\Omega_2}{2}\hat{\sigma}_z\left(\sin^2\Omega_1 t + \frac{1}{2}\right) \\ &- \frac{\Omega_2}{2}(\hat{\sigma}_1\sin\Omega_1 t - \hat{\sigma}_y\sin 2\Omega_1 t) \\ &+(\Delta-\omega_1)(\hat{\sigma}_z\cos\Omega_1 t + \hat{\sigma}_y\sin\Omega_1 t) \\ &+ \frac{q_0}{4\hbar}\sum_i g_i[(i\hat{\sigma}_y\cos\Omega_1 t + i\hat{\sigma}_z\hat{\sin}\Omega_1 t)b_i^\dagger + \text{H.c.}].\end{aligned} \tag{22}$$

The first three terms on the right-hand side can be easily dropped with assumptions similar to those above. The implications of dropping the fourth term need to be analyzed more carefully, done below in Sec. II D.

2. *Effective Hamiltonian and spectral density*

We note that the Hamiltonian of Eq. (21) has the same (non-RWA) interaction term as in Eq. (6), with modified parameters. We then have the effective Hamiltonian

$$\begin{aligned}\hat{H}_{\text{eff}} &= \frac{\hbar\Delta^{\text{eff}}}{2}\hat{\sigma}_z + \frac{q_0}{2}\hat{\sigma}_x\sum_i g_i^{\text{eff}}(\hat{b}_i + \hat{b}_i^\dagger) \\ &+ \sum_i \hbar\omega_i^{\text{eff}}\hat{b}_i^\dagger\hat{b}_i,\end{aligned} \tag{23}$$

where the new parameters have the form

$$\Delta^{\text{eff}} = \frac{\Omega_2}{2}, \tag{24}$$

$$\omega_i^{\text{eff}} = \omega_i - \omega_1, \tag{25}$$

$$g_i^{\text{eff}} = \frac{g_i}{2}. \tag{26}$$

We see that the two-level system and bosonic energies are tunable by the external drives. Since the coupling has kept its form (up to a factor of 2), this allows for tailoring essentially stronger relative couplings between the system and the environment [18,20].

We also have a new coordinate operator of the environment. To determine its properties we first write down the solution in the rotating frame

$$\hat{V}_{\text{eff}}(t) = \frac{1}{2}\sum_i g_i[\hat{b}_i e^{-i(\omega_i-\omega_1)t} + \hat{b}_i^\dagger e^{i(\omega_i-\omega_1)t}]. \tag{27}$$

Here the energies $\omega_i - \omega_1$ are the effective energies in the rotating basis, which can be negative. The population of these modes can be determined from the thermal population in the laboratory frame. Using the spectral density in the original frame $J(\omega)$, we get for the thermal average of the correlation function

$$\langle\hat{V}_{\text{eff}}(t)\hat{V}_{\text{eff}}(0)\rangle_\omega = \frac{\hbar}{2}\frac{J(\omega+\omega_1)}{1-\exp\left(-\frac{\hbar(\omega+\omega_1)}{k_B T}\right)}. \tag{28}$$

The temperature T is the real temperature of the bath. In the following, it is safe to assume that the real bath is at zero temperature since practically $\omega_1 \gg k_B T/\hbar$. We have then

$$\langle\hat{V}_{\text{eff}}(t)\hat{V}_{\text{eff}}(0)\rangle_\omega = \frac{\hbar}{2}J(\omega+\omega_1). \tag{29}$$

In order to have an exact connection between the effective system in the rotating frame and the spin-boson model, the created correlation function in the rotating frame has to simulate a finite-temperature bath. To construct a specific spectral function in the rotating frame with an effective temperature T_{eff}, the spectral density in the laboratory frame is required to have a contribution ($\delta\omega > 0$) below the frequency of the rotating frame,

$$J(\omega_1-\delta\omega) = J(\omega_1+\delta\omega)\frac{1-\exp\left[-\frac{\hbar\delta\omega}{k_B T_{\text{eff}}}\right]}{\exp\left[\frac{\hbar\delta\omega}{k_B T_{\text{eff}}}\right]-1}. \tag{30}$$

If this is satisfied for certain $T_{\rm eff}$, we have

$$\langle[\hat{V}_{\rm eff}(t),\hat{V}_{\rm eff}(0)]_+\rangle_\omega = 2\hbar J_{\rm eff}(\delta\omega)\coth\frac{\hbar\delta\omega}{2k_BT_{\rm eff}}, \quad (31)$$

where we have defined the effective spectral density in the rotating frame

$$J_{\rm eff}(\delta\omega) = \frac{1}{4}J(\omega_1+\delta\omega)\left\{1-\exp\left[-\frac{\hbar\delta\omega}{k_BT_{\rm eff}}\right]\right\}. \quad (32)$$

For $T_{\rm eff}=0$ we have simply

$$J_{\rm eff}(\delta\omega) = \tfrac{1}{4}J(\omega_1+\delta\omega). \quad (33)$$

We note that even though the connection between these two systems might seem trivial, just a frequency shift due to the external drive, it is quite remarkable since it connects two completely different many-body physics problems: one problem including emission and absorption of photons with same bosonic modes and another problem which includes only dissipation to two different set of bosonic modes. The only property that needs to be satisfied to connect these two problems is the effective detailed balance (30).

D. Error estimation

Here we sum up the restrictions and the size of errors in the quantum simulation that appear due to the approximations taken when deriving the effective rotating-frame Hamiltonian. Errors occur from dropping the terms in Eqs. (19) and (22). Furthermore, errors also occur due to a finite anharmonicity of the two-level system, which can lead to a finite population of the third level of the superconducting qubit.

Most terms in Eqs. (19) and (22) can be dropped within the assumptions $\Omega_i/\omega_i \ll 1$ and $(\omega_1-\Delta)/\Omega_1 \ll 1$, as well as $\Omega_2/\Omega_1 \ll 1$. These conditions are easily realized in an experiment [20]. However, the most important contribution we neglected was the term

$$\hat{O} = \frac{q_0}{4}\sum_i g_i[(i\hat{\sigma}_y\cos\Omega_1 t + i\hat{\sigma}_z\sin\Omega_1 t)b_i^\dagger + \text{H.c.}]. \quad (34)$$

This sets a limit to the spectral width and the cutoff of the bath since the term probes the bath in a completely similar way as the central term

$$\frac{q_0}{4}\sum_i g_i\hat{\sigma}_x(\hat{b}_i^\dagger+\hat{b}_i), \quad (35)$$

in the effective Hamiltonian of Eq. (23), but with energies $\Omega_1 \pm \Omega_2/2 \approx \Omega_1$.

To be more quantitative, let us assume that we have a residue bath density at frequencies close to Ω_1, which we now write in the form

$$J_{\rm eff}(\Omega_1) \approx \frac{2\pi\hbar}{q_0^2}\bar{\alpha}\frac{\Omega_2}{2}. \quad (36)$$

The dimensionless variable $\bar{\alpha}$ then compares the effective qubit frequency $\Omega_2/2$ to the spectral density at frequency Ω_1. This gives a bath-induced decoherence rate

$$\frac{\bar{\Gamma}}{\Omega_2/2} \approx \pi\bar{\alpha}. \quad (37)$$

In order to have a negligible contribution within the timescale of the effective two-level system oscillations $1/\Omega_2$, we require that $\bar{\alpha} \ll 1$. Similarly, also a finite internal lifetime of the two-level system, due to internal decay mechanisms, limits the simulation length. Let us denote this rate by $\Gamma_{\rm internal}$. Ideally, we would then like to engineer a bath which does not limit the decay and dephasing times of the qubit itself, i.e., we would like to be in the regime $\bar{\Gamma} < \Gamma_{\rm internal} \ll \Omega_2/2$.

The second important restriction to the parameter regime is the finite anharmonicity of the qubit. The anharmonicity is defined as the difference between the first and second energy-level splittings

$$\hbar\Delta_{\rm an} = |(E_2-E_1)-(E_3-E_2)|. \quad (38)$$

Too strong driving can induce transitions to the third state of the artificial atom. The probability for the artificial atom contributing through the third excited state is roughly

$$P_{\rm error} \sim \left(\frac{\Omega_1}{\Delta_{\rm an}}\right)^2. \quad (39)$$

Therefore, a large anharmonicity qubit is favorable in order to avoid a strong additional upper bound in Ω_1. The qubit anharmonicity depends on the experimental realization. Flux-based qubits can easily reach anharmonicities higher than the lowest-energy-level splitting $\Delta_{\rm an} > \Delta$. In this article we consider a realization based on a transmon qubit with $\Delta_{\rm an} \ll \Delta$ for its simple operation without the necessity of biasing [54], the feasibility of a straightforward capacitive coupling, and its superior coherence properties. For a qubit with $\Delta = 2\pi\times 7$ GHz and anharmonicity $\Delta_{\rm an} = 2\pi\times 350$ MHz, a drive with $\Omega_1 = 2\pi\times 80$ MHz leads to a reasonably low error $P_{\rm error}\sim 0.05$. Combining this with the above analysis, this would also mean that the bath spectral width has to be smaller than 80 MHz in order to avoid unwanted transitions due to the term in Eq. (34). We would then desire a bath that has a rather sharp cutoff at $\omega_c < \Omega_1 = 2\pi\times 80$ MHz, $F_c(\omega)\sim\Theta(\omega_c-\omega)$. Later, in Sec. IV, we show how to build such a bath from a set of microwave resonators.

III. IMPLEMENTATION OF THE SPIN-BOSON MODEL WITH A MICROWAVE CIRCUIT

In this section we study how a superconducting qubit connected to a dissipative microwave-circuit element can be used to realize the spin-boson Hamiltonian. We consider explicitly the case of a transmon qubit. Our main goal is to determine how the parameters of the spin-boson model, the spectral density $S(\omega)$, the coupling q_0, and the qubit energy Δ depend on the properties of the microwave circuit. Section III A briefly sums up the central results. In Sec. III B we describe how to determine the effect of capacitance renormalization in circuits considered in this article. In Sec. III C we detail the derivation of the spin-boson parameters q_0 and Δ and in Sec. III D we show the derivation of the Kondo parameter α. The approach we use is based on a linear circuit analysis, but the results can also be derived by an exact Lagrangian quantization [60–65]. In addition, we provide also a consistency check based on the Born-Markov approach, in Sec. III B. Even though we explicitly consider a transmon qubit, our formalism is generic

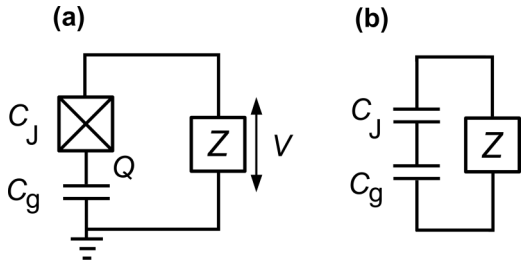

FIG. 2. (a) Model of a transmon qubit connected to an impedance $Z(\omega)$. The charge Q on the island between the Josephson junction (crossed box) and the ground capacitor C_g is a conjugated variable to the phase across the Josephson junction, providing anharmonic energy levels and an effective two-level system. The impedance Z induces voltage fluctuations V and dissipation. (b) Circuit that defines the spectral density [Eqs. (41)–(43)].

and can be extended, in principle, to all superconducting qubit architectures.

A. Spectral density and the system-bath interaction

Our superconducting qubit couples to environmental voltage fluctuations $\hat{V}(t)$, which causes dissipation. The quantity that describes its effect is the spectral density $S(\omega) = \langle \hat{V}(t)\hat{V}(0)\rangle_\omega$. There are several equivalent ways of determining this quantity for microwave circuits, which basically all seek the eigenmodes of the relevant (noninteracting) linear system. In this article we assume that we know the impedance $Z(\omega)$ of the linear circuit connected to the superconducting qubit, an example being the circuit we consider in Sec. IV. Guidelines for a determination of the spectral density in open circuits is given in Appendix A as well as in Refs. [60–65].

Voltage fluctuations across the impedance are described by the operator $\hat{V}$. The exact circuit diagram of the considered setup is shown in Fig. 2(a). Generally, voltage fluctuations in a linear (free-evolution) electric circuit satisfy the quantum fluctuation-dissipation theorem [56]

$$\langle \hat{V}(t)\hat{V}(0)\rangle_\omega = \frac{2\hbar\omega\,\mathrm{Re}[Z_{\mathrm{eff}}(\omega)]}{1-e^{-\beta\hbar\omega}}. \tag{40}$$

In this free-evolution solution, where the transmon island charge is set to zero (see below), the impedance $Z(\omega)$ sees a parallel capacitance C_{int}, which is the effective qubit capacitance [56,66,67]

$$C_{\mathrm{int}} = \left(C_J^{-1} + C_g^{-1}\right)^{-1}. \tag{41}$$

Here C_J and C_g denote the capacitances of the Josephson junction and the capacitance to ground, respectively. The effective impedance of the environment, to be used in Eq. (40), assumes the form

$$Z_{\mathrm{eff}}^{-1}(\omega) = i\omega C_{\mathrm{int}} + Z^{-1}(\omega). \tag{42}$$

The equivalent circuit is shown in Fig. 2(b). Note that the inductance of the Josephson junction, which determines the qubit dynamics, does not enter the calculation of $Z_{\mathrm{eff}}^{-1}(\omega)$ but only the effective qubit capacitance C_{int} that shunts the effective bath impedance.

We also note that the scenario where a bath circuit is used to tailor a dissipative qubit environment is fundamentally different from the case where a certain impedance is used to filter microwave transmission. The reason is a different boundary condition at the qubit: In the case of the tailored bosonic environment, radiation reflects at the capacitor C_{int}, whereas in the case of a microwave filter, we would have an impedance-matched load and no reflection.

A direct comparison of Eqs. (9) and (40) yields the relation between the spectral density of the spin-boson model and the effective impedance

$$J(\omega) = \omega\,\mathrm{Re}[Z_{\mathrm{eff}}(\omega)]. \tag{43}$$

This equation is central for experimentally tailoring a bosonic environment, relating the effective impedance to the resulting spectral density $J(\omega)$. It has also been shown recently that the parallel contribution C_{int} in the spectral density is indeed an essential quantity for a consistent description of such systems in all parameter regimes [64,65].

In the considered circuit, the transmon interacts with the environmental voltage fluctuations through the operator [66,67]

$$\hat{H}_{\mathrm{int}} = \beta\hat{Q}\hat{V} \equiv \hat{Q}_{\mathrm{int}}\hat{V}, \tag{44}$$

$$\beta = \frac{C_g}{C_J + C_g}. \tag{45}$$

Here $\hat{Q}$ is the charge operator of the transmon island. The interaction charge $\hat{Q}_{\mathrm{int}}$ accounts for an internal transmon-qubit capacitive shunting through parameter β, reducing the coupling to the island charge $\hat{Q}$ [54]. The parameter β is not affected by renormalization effects. However, for determination of the resulting spin-boson Hamiltonian parameter q_0, one generally needs to consider also the possible qubit-capacitance renormalization due to coupling to the impedance, as analyzed in Sec. III B. The final result reads

$$q_0 = 2e\beta\sqrt{\frac{R_Q}{\pi Z_J}}. \tag{46}$$

Here the characteristic impedance of the transmon is defined as $Z_J = R_Q\sqrt{2E_C/\pi^2 E_J}$, where E_J is the Josephson coupling energy, $E_C = e^2/2(C_J + C_g^0)$ is the charging energy, and the effective ground capacitance C_g^0 depends on the realization (see Sec. III B). In the simplest case $C_g^0 = C_g$. Finally, the normalized two-level system energy Δ for typical transmon parameters becomes [54]

$$\Delta \approx \frac{1}{\hbar}\sqrt{8E_J E_C}. \tag{47}$$

In the following section we show how to determine E_C and demonstrate that the given identifications are consistent with the alternative approach of including the interaction term of Eq. (44) using a Born-Markov approximation. It is also consistent with the exact derivation when using an open circuit, given in Appendix A.

B. Capacitance renormalization

The impedance $Z(\omega)$ can affect the Hamiltonian of the transmon. The effect is generally twofold: It renormalizes (i) the effective transmon capacitance and (ii) the Josephson coupling energy E_J. Effect (i) is analogous to mass

renormalization in the spin-boson model [1] and here can be significant. Effect (ii) is analogous to tunneling-amplitude renormalization in the spin-boson model, before going into the spin-boson representation [1], and here stays small due to small environmental impedances considered $Z \ll R_Q$ and low qubit energies in comparison to the superconducting energy gap.

1. Hamiltonian of an isolated transmon

The Hamiltonian of a superconducting artificial atom can be derived by applying a Lagrangian formalism to electric circuits [68]. The Hamiltonian of an isolated transmon is of the form [54]

$$\hat{H}_{\rm tr}^{\rm isolated} = -E_J \cos\hat{\varphi} + \frac{\hat{Q}^2}{2(C_J + C_g)}. \tag{48}$$

The first term on the right-hand side describes Cooper-pair tunneling across the superconducting junction as a function of the superconducting phase difference $\hat{\varphi}$ across the Josephson junction. The second term describes the capacitive (Coulomb) energy related to the island charge Q. In this isolated circuit, the effective island capacitance is the sum of C_J and C_g. The phase and the charge are conjugated variables

$$\left[\frac{\hat{Q}}{2e}, e^{i\hat{\varphi}}\right] = e^{i\hat{\varphi}}. \tag{49}$$

The commutation relation is presented in this (periodic) form since the island charge takes only values that are multiples of $2e$ or, equivalently, the phase distribution here is by definition 2π periodic.

2. Accounting for the counterterm

Finding the capacitance renormalization is analogous to identifying the counterterm in general system-reservoir models [1,2]. In this analysis, we study two equivalent forms of the total Hamiltonian

$$\hat{H}_{\rm total} = \hat{H}_{\rm tr} + \hat{H}_{\rm bath} + \hat{H}_{\rm int}, \tag{50}$$

$$\hat{H}_{\rm total} = \hat{H}_{\rm tr}^0 + \hat{H}_{\rm bath} + [\hat{H}_{\rm int} + \hat{H}_{\rm ct}], \tag{51}$$

where then

$$\hat{H}_{\rm tr}^0 = \hat{H}_{\rm tr} - \hat{H}_{\rm ct}. \tag{52}$$

In addition to the qubit, bath, and interaction Hamiltonians, we have introduced a term $\hat{H}_{\rm ct}$, counteracting the qubit Hamiltonian renormalization (coherent embedding of the environment) coming from the interaction term $\hat{H}_{\rm int}$. It is here the interaction-normalized Hamiltonian $\hat{H}_{\rm tr}^0$ that should be used when theoretically reducing the transmon to a two-level system and whose dynamics is observed in the experiment.

Strictly speaking, the renormalization is determined theoretically by first evaluating the Hamiltonian of Eq. (50), for example, by using a Lagrangian approach (Appendix A) and then estimating the embedding due to the interaction term $\hat{H}_{\rm int} = \hat{Q}_{\rm int}\hat{V}$. However, we find that in circuits we consider the contributions $\hat{H}_{\rm ct}$, $\hat{H}_{\rm tr}$, and $\hat{H}_{\rm tr}^0$ can be deduced more straightforwardly from the following coherent solutions: (a) the solution when the resistor lead is connected but its resistivity is set to zero, giving $H_{\rm tr}^0$, and (b) the solution when the resistive part is disentangled from the circuit, for example, with an additional capacitor $C_{\rm dis} \to 0$ in series with the resistor, giving $H_{\rm tr}$.

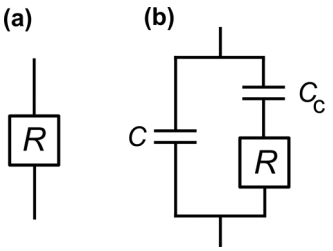

FIG. 3. Two environmental impedances $Z(\omega)$, whose capacitance renormalization is considered explicitly in this section.

To illustrate the mathematics of this approach, let us consider the simple case of a bare Ohmic impedance $Z(\omega) = R$. We first identify the Hamiltonian of the circuit when resistivity is set to zero. This fully coherent system corresponds to the one in Eq. (48),

$$\hat{H}_{\rm tr}^0 = \hat{H}_{\rm tr}^{\rm isolated}. \tag{53}$$

In the second stage, we identify the transmon Hamiltonian when disconnected from the resistor lead, which has the form (Appendix A)

$$\hat{H}_{\rm tr} = -E_J \cos\hat{\varphi} + \frac{\hat{Q}^2}{2C_J}. \tag{54}$$

Using this, we find for the difference

$$\begin{aligned}\hat{H}_{\rm ct} &= \hat{H}_{\rm tr} - \hat{H}_{\rm tr}^0 \\ &= \frac{\hat{Q}^2}{2C_J} - \frac{\hat{Q}^2}{2(C_J + C_g)} = \frac{\hat{Q}_{\rm int}^2}{2C_{\rm int}}.\end{aligned} \tag{55}$$

Let us now consider the circuit shown in Fig. 3(b), which is analogous to our proposal presented in Sec. IV. When the resistance is set to zero, an environmental capacitive remains with contribution $C + C_c$, leading to

$$\hat{H}_{\rm tr}^0 = -E_J \cos\hat{\varphi} + \frac{\hat{Q}^2}{2\left(C_J + C_g^0\right)}, \tag{56}$$

where

$$C_g^0 = \left[C_g^{-1} + (C + C_c)^{-1}\right]^{-1}. \tag{57}$$

In the second stage, we get for the Hamiltonian corresponding to the disconnected resistor

$$\hat{H}_{\rm tr} = -E_J \cos\hat{\varphi} + \frac{\hat{Q}^2}{2(C_J + C_{g'})}, \tag{58}$$

where we have defined an effective gate capacitance

$$C_{g'} = \left(C_g^{-1} + C^{-1}\right)^{-1}. \tag{59}$$

This is since C appears in a series connection with C_g. To evaluate the counterterm, let us consider explicitly the case $C \to 0$. We get for the difference

$$\begin{aligned}\hat{H}_{\rm ct} = \hat{H}_{\rm tr} - \hat{H}_{\rm tr}^0 &= \frac{\hat{Q}^2}{2(C_J + C_{g'})} - \frac{\hat{Q}^2}{2\left(C_J + C_g^0\right)} \\ &= \frac{C_c}{C_c + C_{\rm int}} \frac{1}{2C_{\rm int}} \hat{Q}_{\rm int}^2.\end{aligned} \tag{60}$$

To show that the above results are sound, we can estimate the embedding due to the interaction term $\hat{H}_{\rm int} = \hat{Q}_{\rm int}\hat{V}$ by an alternative method, using a Born-Markov master equation. Such an approach assumes that the effect of the environment (beyond the counterterm) is weak, but its result is valid also more generally since the embedding of the environment is the same for all R. Here we start from the Hamiltonian $\hat{H}_{\rm tr}$, where the resistor lead is decoupled from the transmon, and estimate the renormalization explicitly. Considering the circuit of Fig. 3(a), we then use the property that for an Ohmic environment with resistance R and cutoff defined by the parallel capacitor $(RC_{\rm int})^{-1} = \omega_c$, we have transition rates and energy-level renormalization terms

$$\lim_{s\to 0}\int dt\, e^{i(\omega+is)t}\langle\hat{V}(t)\hat{V}(0)\rangle = \frac{\hbar\omega}{1-e^{-\beta\hbar\omega}}{\rm Re}[Z(\omega)] - i\frac{\hbar\omega_c}{2}{\rm Re}[Z(\omega)] + i\frac{\hbar\omega}{2\pi}{\rm Re}[Z(\omega)]\tilde{\Psi}(\omega), \quad (61)$$

where ${\rm Re}[Z(\omega)] = R/[1+(\omega/\omega_c)^2]$ and $\tilde{\Psi}(\omega)$ is defined by a digamma function [67]. The last (imaginary) contribution is for practical systems, with finite temperatures, of the same size as the real part: It stays small for environments inducing weak transition rates for the laboratory-frame qubit, which we assume to be true in this article. More specifically, this extra contribution is assumed to be small compared to the anharmonicity of the qubit. The other (and possibly large) imaginary term is independent of the resistance at usual frequencies which are well below ω_c and produces a constant $-i/2C_{\rm int}$. As this enters a master equation through the matrix elements of $\hat{Q}_{\rm int}$, one obtains finally a coherent renormalization term $Q_{\rm int}^2/2C_{\rm int}$, as obtained also in Eq. (55). This is the desired result. In the same way, such consistency of the capacitance renormalization between the two approaches can also be shown to hold for the circuit of Fig. 3(b) with a counterterm as in Eq. (60). The analysis of this section also holds exactly for $C > 0$.

C. Parameters Δ and q_0 for a transmon qubit

After theoretically identifying the capacitance renormalization caused by the environment to the superconducting artificial atom, we reduce the transmon to a two-level system using the Hamiltonian $\hat{H}_{\rm tr}^0$ [Eq. (52)]. We can now make a connection between the parameters of the transmon qubit and the spin-boson parameter q_0.

For typical transmon parameters, the energy-level difference between the ground and the first excited state is

$$\Delta \approx \frac{1}{\hbar}\sqrt{8E_JE_C}. \quad (62)$$

Here, for example, for the Hamiltonian of Eq. (56) the charging energy $E_C = e^2/2(C_J + C_g^0)$. The transmon is practically a nonlinear resonator, which reduces to a two-level system when maximally only the two lowest-energy levels are populated. The relevant quantity describing this reduction is the anharmonicity (difference between the first and the second energy-level differences)

$$\hbar\Delta_{\rm an} = E_2 - E_1 - (E_3 - E_2) \approx E_C. \quad (63)$$

This variable will play an important role in a practical realization, since the drive amplitudes Ω_i of Eq. (16) need to be smaller than the nonlinearity of the qubit, as discussed in Sec. II D.

The transverse matrix element of the operator $\hat{Q}$, on the other hand, is

$$|\langle\downarrow|\hat{Q}|\uparrow\rangle|^2 = e^2\sqrt{\frac{E_J}{2E_C}} = e^2\frac{R_Q}{\pi Z_J}. \quad (64)$$

Applying the result of Eq. (64) and comparing to the form of the spin-boson Hamiltonian of Eq. (6), we get the connection

$$\hat{Q}_{\rm int} = \beta\hat{Q} = \beta e\sqrt{\frac{R_Q}{\pi Z_J}}\hat{\sigma}_x \equiv \frac{q_0}{2}\hat{\sigma}_x, \quad (65)$$

where now

$$q_0 = 2e\beta\sqrt{\frac{R_Q}{\pi Z_J}}. \quad (66)$$

Here again $\beta = C_g/(C_J + C_g)$, where the ground capacitance is the unnormalized (original) one C_g, whereas in the definition of the charging energy and system energy levels the effective ground capacitance C_g^0 appears.

D. Parameter α for a transmon qubit (Ohmic spectral density)

A central situation in the spin-boson theory is the case of an Ohmic environment. Assuming an Ohmic impedance ${\rm Re}[Z_{\rm eff}] = R$, we have $J(\omega) = R\omega \equiv \eta\omega$. This yields a Kondo parameter

$$\alpha = \frac{1}{\pi}\beta^2\frac{R}{Z_J}. \quad (67)$$

The coupling α scales linearly with R and is reduced by the capacitive shunting by the ground capacitance ($\beta < 1$). The relevant quantity to compare R is the characteristic impedance of the Josephson junction Z_J. The size of α when realized in the rotating frame is studied in Sec. IV.

Moreover, for a transmon qubit and for $\alpha \ll 1$ (weak-coupling limit) there is a direct connection between α and the quality factor of the qubit. A golden rule calculation gives for the decay rate [3] (inverse quality factor)

$$\frac{\Gamma_\downarrow}{\Delta} = \beta^2\frac{R}{Z_J} = \pi\alpha. \quad (68)$$

The limit $\beta = 1$ (no shunting of voltage fluctuations) is the result for a dissipative classical resonator. This direct connection appears since we have treated the transmon as a harmonic oscillator, with weak nonlinearity, which is a good approximation since $E_J \gg E_C$. The relation between the energy decay rate $\Gamma_\downarrow$ and the spin-boson parameter α was studied recently in Ref. [49] in the case of a high-anharmonicity flux qubit coupled to an open transmission line.

We note that if we would consider the Cooper-pair box qubit, working in the limit $E_J \ll E_C$, we would have $q_0 = 2e$, leading to $\alpha = R/R_Q$. There, a resistance $R = R_Q$ is needed to reach $\alpha = 1$.

IV. TAILORING AN OHMIC BATH IN THE ROTATING FRAME

In this section we consider constructing an Ohmic bath in the rotating frame from multiple microwave resonators with broadening. Each such resonator can be, for example, a superconducting lumped element LC resonator integrated with a resistive element R or a superconducting coplanar resonator with a leakage to an open transmission line. After a qualitatively analysis of the achievable Kondo parameter α (Sec. IV A), we introduce our method and show a numerical example of the bath construction (Sec. IV B). Analytical relations for bath properties are derived in Sec. IV C and robustness against parasitic coupling between neighboring resonators is analyzed in Sec. IV D.

A. Ohmic spectral density in the rotating frame

Let us first apply the idea presented in Sec. II C to realize an effective Ohmic environment in the rotating frame. We first note that in our effective system

$$\omega_c \ll \omega_1, \tag{69}$$

where ω_1 is the dominant Rabi frequency, which is tuned to the energy of the superconducting qubit, $\Delta \sim 2\pi \times 7$ GHz, and the cutoff frequency $\omega_c \lesssim 2\pi \times 100$ MHz. This means that we practically need a linearly increasing impedance to create a linearly increasing $J_{\rm eff}(\omega)$, since here $J(\omega) = \omega\,{\rm Re}[Z(\omega)] \approx \omega_1 {\rm Re}[Z(\omega)]$.

Let us now assume that a parameter $R = \eta$ in some Ohmic environment of the original system describes also the maximum value of the spectral density in the constructed effective system. Practically, such a parameter corresponds to a characteristic impedance of the microwave transmission line or resonator. In this discussion, for simplicity, we neglect the factor 4 difference between the laboratory-frame and the rotating-frame spectral densities. Let us denote by ω_q the frequency where the maximal impedance is reached in the effective system and the two impedances meet, so we have $J(\omega_q) = R\omega_q$, as depicted in Fig. 4. This gives for the coupling parameter in the rotating frame

$$\eta_{\rm eff} = R\frac{\omega_q}{\omega_q - \omega_1} = R\left(1 + \frac{\omega_1}{\omega_c}\right). \tag{70}$$

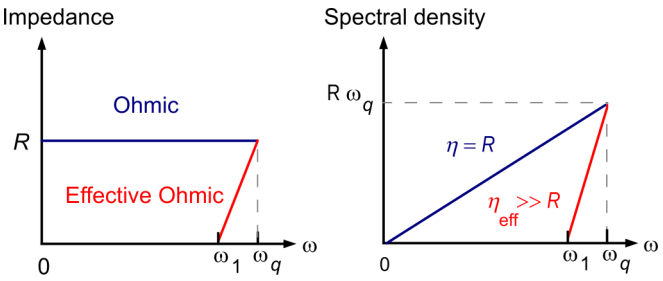

FIG. 4. Qualitative forms of the impedance Re$[Z(\omega)]$ and spectral density $J(\omega)$ of two different environments, one being Ohmic in the laboratory frame (blue lines) and one being Ohmic in the rotating frame (red lines). For the same value of impedance at a certain frequency $\omega_q \gtrsim \omega_1$, Re$[Z(\omega_q)] = R$, the coupling parameter $\eta = \partial J(\omega)/\partial\omega$ can be essentially larger in the rotating frame.

We see that establishing a linear increase of $J(\omega)$ in the rotating frame, we can realize an essentially larger $\eta_{\rm eff}$, with the same maximal impedance R. It can also be interpreted that the impedance of the environment is effectively increased, without a change in the material design.

By applying this idea for a system with a transmon qubit we then get for the effective coupling in the rotating frame (accounting for the factor 4)

$$\alpha_{\rm eff} = \frac{\beta^2}{4\pi}\frac{\eta_{\rm eff}}{Z_J} = \frac{\beta^2}{4\pi}\frac{R}{Z_J}\left(1 + \frac{\omega_1}{\omega_c}\right). \tag{71}$$

The individual multiplied contributions play an important role in determining the magnitude of $\alpha_{\rm eff}$. The term $\beta^2/4\pi$ reduces the coupling at least by an order of magnitude. Also the (maximal) resistivity needs to be relatively small, $R/Z_J < 1$. If we assume that these two contributions reduce the coupling by two to three orders of magnitude, then (in this example) it is the role of the term $1 + \omega_1/\omega_c \approx \omega_1/\omega_c$ to counteract this contribution. For example, we would need $\omega_1/\omega_c \approx 10^2$ in order to reach very strong couplings $\alpha_{\rm eff} \sim 0.1$–$1$. This corresponds to a relatively narrow-bandwidth environment $\omega_c \lesssim 2\pi \times 100$ MHz. This qualitative demand should be considered together with the restriction to drive strengths Ω_1 that are much weaker than the transmon qubit anharmonicity $\Delta_{\rm an} \lesssim 2\pi \times 350$ MHz and that the Rabi frequency has to be above the cutoff of the effective environment $\Omega_1 > \omega_c$ (see Sec. II D).

B. Bath engineering with multiple resonators

In this work we consider constructing the environmental impedance by using a set of LCR resonators, each of them coupled through a coupling capacitor C_{ci}, as shown in Fig. 5. We desire a method that is based on a feasible manipulation of resonator parameters. Possible methods for tailoring the spectral density are varying the individual couplings of the resonators to the qubit and varying the spacings between the resonance

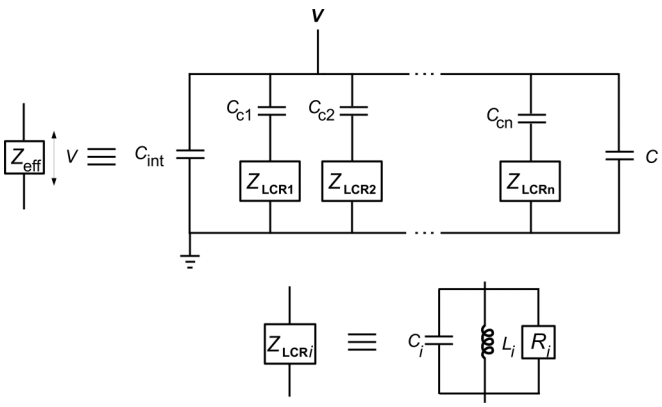

FIG. 5. We consider constructing the bosonic environment from multiple LCR resonators coupled capacitively to a superconducting qubit. Each resonator can be a superconducting lumped element LC resonator integrated with a resistive element R or, for example, a superconducting coplanar resonator with leakage to an open transmission line. The qubit itself contributes to the effective impedance through the interaction capacitance $C_{\rm int}$ [Eq. (41)]. The resonators are also assumed to be in parallel with an extra capacitor C, describing the coupling of the qubit antenna to ground.

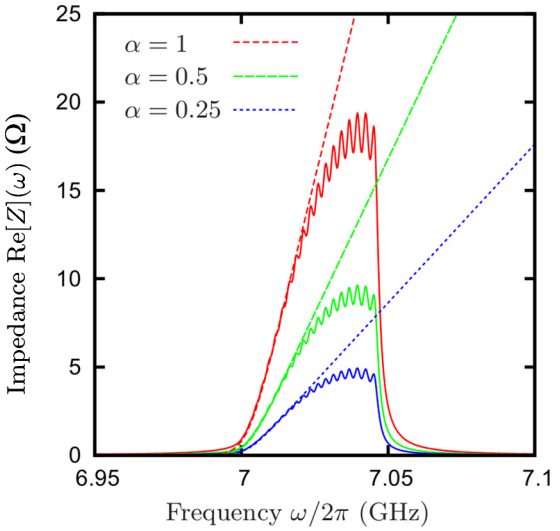

FIG. 6. Effective Ohmic spectral density with three different Kondo parameters α in the rotating frame at $\omega_1/2\pi = 7$ GHz. The impedance is constructed from $N = 20$ dissipative resonators with internal $Q \approx 2.2 \times 10^3$. A linear decrease in bath impedance Re[$Z(\omega)$] is obtained here by reducing the coupling capacitance from 0.5 fF quadratically to zero [$\sim 1 - (i-1)^2/N^2$, where i is the number of the resonator] while increasing the inductance linearly (with i). Different couplings α correspond to different parallel capacitors C such that $C + C_{\rm int}$ takes the values 70 fF ($\alpha = 1$), $\sqrt{2} \times 70$ fF ($\alpha = 1/2$), and 2×70 fF ($\alpha = 1/4$). The used transmon parameters are $Z_J = 200\ \Omega$, $\beta = 1/\sqrt{2}$, and resonator $Z_{LC} \approx 113\ \Omega$.

frequencies. A general recipe that can be implemented in an experiment is the following.

(i) Realize all resonators with slightly different frequencies, by varying their inductances L_i and/or capacitances C_i.

(ii) Shape the spectral function by changing individual coupling capacitances C_{ci} and/or resonance-frequency spacing.

The resonator broadenings, defined by variables R_i, can be used to shape the spectral function of the bath as well, but more importantly it is closely connected to the achievable Kondo parameter α, as shown below.

A practical example of bath shaping using our approach is shown in Fig. 6, where an effective Ohmic impedance is constructed from $N = 20$ resonators by varying inductances L_i and coupling capacitances C_{ci}. A straightforward method for calculating the total impedance (and thereby the spectral function) of similar circuits is given in Appendix C.

C. Analytical relations

More fundamental connections between the chosen parameters and the achievable spectral density exists. Below we first show analytically how the broadening and coupling of individual modes relate to α. After this we consider explicit formulas for the size of the individual couplings and study how the size of the constructed (smooth) impedance depends on resonator properties and the resonance-frequency density. We also estimate the size of the transmon-capacitance renormalization.

1. Kondo parameter α

Let us first analyze how the linear increase of spectral density relates to the coupling to individual broadened resonators. It is reasonable to assume that the steepness of the spectral density at low effective frequencies (see, for example, Fig. 6) is similar to, or limited by, the spectral steepness related to the individual broadened resonators. The following discussion is made for a laboratory-frame system, but the qualitative result is independent of the chosen frame.

We then evaluate the decay rate of the qubit due to single environmental broadened resonator. According to the golden rule, the decay rate is

$$\Gamma = \frac{\gamma}{\gamma^2 + 4\omega^2} g^2, \tag{72}$$

where γ is the width (decay rate) of the resonator, ω the frequency with respect to the resonance frequency, and $g \equiv q_0 g_i/\hbar$ the total coupling. The result for the decay rate is strictly valid for small couplings $g \ll \gamma$, but this formula indeed provides a general connection between an individual resonator spectral density and a coupling to the qubit. The derivative of the golden rule decay rate is

$$\frac{\partial\Gamma}{\partial\omega} = -8\left(\frac{g}{\gamma}\right)^2 \frac{\frac{\omega}{\gamma}}{\left[1 + 4\left(\frac{\omega}{\gamma}\right)^2\right]^2}. \tag{73}$$

This has a maximal value $\gtrsim (g/\gamma)^2$. Assuming that we synthesize a linear increase of the spectral density which qualitatively follows this steepness, we can relate this directly to the parameter α,

$$\frac{\partial\Gamma}{\partial\omega} = \pi\alpha \sim \left(\frac{g}{\gamma}\right)^2. \tag{74}$$

We then find that for couplings $\alpha \sim 1$ at least some of the resonators are in the strong-coupling regime ($g \sim \gamma$). It is, however, not needed that individual resonators are in the ultrastrong-coupling regime. This seemingly fundamental result states that the onset of the single-resonator strong-coupling regime, which comes together with the non-Markovian system-environment interaction, is closely related to the strong coupling in the spin-boson model ($\alpha \sim 1$), when the environment is constructed from multiple resonators.

2. Coupling to individual resonators

Let us consider now how the coupling to an individual resonator g relates to the system parameters. Here a Hamiltonian for the qubit coupled to a single (nondissipative) resonator with inductance L_1 and capacitance C_1 is of the form

$$H \approx \frac{\hbar\Delta}{2}\hat{\sigma}_z + \hbar\omega_1 \hat{b}^\dagger \hat{b} - \frac{1}{2}\beta\frac{C_c}{C + C_{\rm int}} \times \sqrt{\frac{C_T}{C_1}}\hbar\sqrt{\Delta\omega_1}(\hat{b}^\dagger - \hat{b})(\hat{\sigma}_+ - \hat{\sigma}_-), \tag{75}$$

where $\hbar\Delta = \sqrt{8E_J E_C}$, $E_C = e^2/2C_T$, $C_T = C_J + CC_g/(C + C_g)$, $\omega_1 = 1/\sqrt{L(C_1 + C_c)}$, and we have assumed that $C_c \ll C_J, C_1, C_g$. For equal system frequencies $\Delta = \omega_1$ we get

$$g = \beta\frac{C_c}{C + C_{\rm int}}\sqrt{\frac{C_T}{C_1}}\Delta. \tag{76}$$

A practical example is $\beta = 1/\sqrt{2}$, $C_c = 0.1$ fF, $C + C_{\rm int} = 70$ fF, $C_1 = 2C_T = 200$ fF, and $\Delta/2\pi = 7$ GHz, which gives $g/2\pi = 5$ MHz. In the rotating frame the coupling is halved to 2.5 MHz.

When constructing the spectral density using multiple resonators with internal losses, the coupling to individual resonators is reduced. This is due to the collective capacitance due to all other resonators

$$C_c^{\rm total} \equiv \sum_{i=1}^{N} C_{ci}. \tag{77}$$

We assume here that $N \gg 1$, so the considered resonator can be included in the sum with negligible error. The effect of coupling to a single resonator is the same as increasing the extra capacitance to ground as $C \to C + C_c^{\rm total}$. The coupling to qubit is then approximately

$$g = \beta \frac{C_c}{C + C_{\rm int} + C_c^{\rm total}} \sqrt{\frac{C_T}{C_1}} \Delta. \tag{78}$$

Here also $\hbar\Delta = \sqrt{8E_J E_C}$ and $E_C = e^2/2C_T$, but now with $C_T = C_J + (C + C_c^{\rm total})C_g/(C + C_c^{\rm total} + C_g)$.

3. Value of constructed smooth impedance

Let us now study the size of impedance synthesized within our method. For this we consider first establishing a rectangular impedance between certain frequencies ω_1 and $\omega_1 + \omega_{\rm interval}$. Two parameter limits lead to simple analytical formulas: (i) when the collective coupling $C_c^{\rm total} \gg C_{\rm int} + C$ and (ii) when $C_c^{\rm total} \ll C_{\rm int} + C$.

Let us first consider the case $C_c^{\rm total} \gg C_{\rm int} + C$. In this case, the effective parallel capacitive shunting is not due to the qubit or the capacitance C but due to all the other resonators. Here, assuming the same coupling capacitance $C_{ci} = C_c$ for all N resonators, we get a reduction of the impedance seen by the qubit of one resonator (due to shunting of the other resonators) by a factor

$$\left(\frac{C_c}{NC_c}\right)^2 = \left(\frac{1}{N}\right)^2. \tag{79}$$

Each resonator contributes to the real part of the effective impedance (before the considered reduction) with a Lorentzian of area $\omega_i Z_{LCi}$ and a width $\delta\omega = \omega_i R_i/Z_{LCi}$, where the characteristic impedance of resonator i is

$$Z_{LCi} = \sqrt{\frac{L_i}{C_i}}. \tag{80}$$

Then the average value of the real part of the environmental impedance is (assuming a nearly constant characteristic impedances and an interval $\omega_{\rm interval} \ll \omega_1$)

$$\begin{aligned} R &\approx \frac{1}{\omega_{\rm interval}} \int_{\omega_1}^{\omega_1+\omega_{\rm interval}} {\rm Re}[Z(\omega)] d\omega \\ &\approx \frac{1}{\omega_{\rm interval}} \left(\frac{1}{N}\right)^2 N\omega_1 Z_{LC} \\ &= Z_{LC} \frac{\omega_1}{\omega_{\rm interval}} \frac{1}{N}. \end{aligned} \tag{81}$$

We see that a fundamental limit is set by the characteristic impedance of the resonators. Indeed, for a typical set of parameters we find numerically that

$$R \sim Z_{LC}. \tag{82}$$

However, the effect of such impedance to the transmon is actually large, since the transmon impedance is usually of the same magnitude, which is not the regime we want to be in.

In the case $C_c^{\rm total} \ll C_{\rm int} + C$, the effective parallel shunting is due to the qubit contribution $C_{\rm int}$ and capacitance C. This is practically the regime of our proposed system. Here the preceding results are valid with an additional reduction factor $[NC_c/(C_{\rm int} + C)]^2$. We then estimate for the (rectangular) impedance achieved by the considered method

$$R \sim \left(\frac{NC_c}{C_{\rm int} + C}\right)^2 Z_{LC} \frac{\omega_1}{\omega_{\rm interval}} \frac{1}{N}. \tag{83}$$

In this regime, the size of the dimensionless coupling parameter α can then be controlled by the capacitance C, which is done in the simulation of Fig. 6.

4. Transmon capacitance renormalization

The environmental impedance can affect the qubit parameters through a capacitance renormalization. Applying the approach described in Sec. III B, we identify the Hamiltonian of the circuit when resistances are set to zero. Here the parallel LCR circuits become effectively shorts. The environmental capacitance as seen by the qubit is then

$$C_{\rm env} = C_c^{\rm total} + C. \tag{84}$$

This fully coherent system corresponds to the Hamiltonian of Eq. (56) with

$$C_g^0 = \left[C_g^{-1} + (C_{\rm env})^{-1}\right]^{-1}. \tag{85}$$

Depending on the size of the term of Eq. (84) in comparison to C_g, the contribution of this can be significant (for example, when $C_{\rm env} < C_g$ and $C_J \sim C_g$). This correction then needs to be included in the free Hamiltonian (56).

We note that the same result is obtained also by reducing the characteristic impedance of resonators to zero, by taking the resonator capacitances to infinity. This gives for the effective capacitance of each resonator lead C_{ci} and thereby again an effective environmental capacitance as in Eq. (84).

D. Robustness against parasitic coupling

Here we numerically study deviations in the spectral function due to a parasitic mutual coupling of bosonic bath resonators. As described in Appendix C, we assume a capacitive nearest-neighbor coupling between resonators, with cyclic boundary conditions. Unwanted substructure that is introduced by this mutual coupling is suppressed when resonators nearby in frequency are arranged also spatially adjacent (except at the boundary from the largest to the smallest). A numerical simulation of the effect of parasitic coupling is provided in Fig. 7. We generally find that the resonator-resonator coupling should be of the same order as or less than the coupling of individual resonators, so that our construction method works. In the opposite limit, the individual peaks are pushed away from each other and become visible. We can then summarize two important findings for tailoring the impedance for Kondo couplings $\alpha \sim 1$ using the presented method.

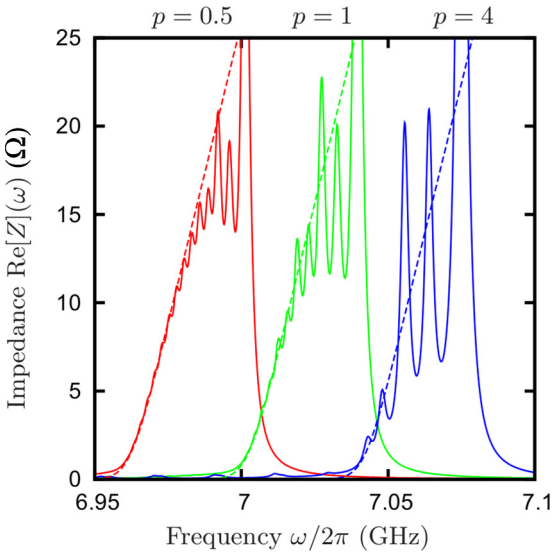

FIG. 7. Effect of parasitic resonator-resonator coupling to the impedance of the system in Fig. 6. Here $p = C_p/C_i^{\max}$ corresponds to the relative strength of the parasitic coupling, where C_p is the nearest-neighbor parasitic capacitance and $C_i^{\max} = 0.5$ fF is the maximal coupling between a resonator and qubit. The other parameters are as in Fig. 6 for $\alpha = 1$. The curves have been separated by 0.04 GHz and the dashed lines correspond to the spectral densities with $\alpha = 1$. We find that the low-frequency part of the impedance is practically unchanged when parasitic coupling is of the same magnitude or less than the (maximal) qubit-resonator coupling.

(a) Coupling between the qubit and at least some of the resonators has to be in the strong-coupling limit $g \sim \gamma$.

(b) Parasitic coupling between resonators should be maximally of the same order as the maximal coupling to the qubit g.

V. EXPERIMENTAL REALIZATION

In this section we provide a brief description of an experimental realization of a spin-boson quantum simulator based on a modular flip-chip approach. In addition, we discuss experimental protocols that allow one to access interesting quantities of the two-level system in the spin-boson simulator. They include the bath initialization, qubit-state preparation, and qubit-state measurement.

A. Flip-chip approach

In our preliminary experimental realization of the spin-boson model, we place the two-level system and the bosonic bath on two physically different chips. Both samples are mounted in a specifically designed sample box on top of each other in a flip-chip fashion [69,70]. The qubit sample at the bottom is mounted on the ground level of the sample box, which allows for the required bond connections to the coaxial control lines, while the upper sample containing the bosonic bath is flipped upside down and therefore facing the qubit chip. The capacitive coupling between the qubit and bosonic bath is mediated via electric fields in the volume between the two samples.

We implement a bosonic bath formed by $N = 20$ lumped-element resonators that individually couple to the qubit via coupling antennas. The resonators are equipped with resistive elements that allow us to tailor their internal dissipation such that they overlap in a restricted frequency band and form a bosonic bath of a smooth spectral function. A shaping of the bosonic bath impedance $Z(\omega)$ is achieved by adjusting the individual coupling strengths between the qubit and the bosonic resonator modes, as described in Sec. IV. The two-level system is formed by a concentric transmon qubit [71], which allows for an approximately equal coupling in any direction in its plane due to its rotational symmetry.

In a preliminary experiment, we have demonstrated that the qubit decay rate can be dominated by the engineered bosonic bath in a spectral range of ∼500 MHz. The bath-induced qubit decay rate at different frequencies corresponded here directly to the noise at different frequencies in the spin-boson model ($\alpha \ll 1$) and thereby shows that quantum simulation using the flip-chip approach is possible. A more detailed description of this experiment is provided in Ref. [70].

B. Measurement protocols

In order to experimentally observe specific dynamics of the spin-boson model, we propose two possible pulse sequences that allow us to access the expectation values of $\hat{\sigma}_x$ [well population function $P(t)$] as well as of $\hat{\sigma}_z$ (energy decay) with different bath initializations. A brief description for the expected behavior of the well-population dynamics, the function $P(t)$, is given in Sec. II B 2 and in Fig. 1.

1. Qubit initialization and measurement of $\langle\hat{\sigma}_z\rangle$ and $\langle\hat{\sigma}_x\rangle$

Observing the time evolution of the expectation values $\langle\hat{\sigma}_z\rangle$ or $\langle\hat{\sigma}_x\rangle$ can be performed with an extension of the measurement protocol applied in Ref. [20] [see Figs. 8(a) and 8(b)]. The qubit in the laboratory frame is initially biased to a frequency outside the spectral location of the bosonic bath. In the frequency space shown in Fig. 8(b), this is referred to as qubit control. The qubit is excited to the equatorial plane of the Bloch sphere by applying a $\pi/2$ rotation [see Fig. 8(a)]. By controlling the relative phase of the successive Rabi drives [20], we can prepare the qubit in an eigenstate of $\hat{\sigma}_x$. This allows us to also initialize the effective qubit state, because at $t = 0$ eigenstates remain unchanged during the transformation into the rotating frame. Alternatively, the qubit can stay in its ground state or be prepared in its excited state by applying a π rotation prior to the start of the simulation sequence at $t = 0$. With a fast frequency tuning pulse, the qubit is brought into resonance with the bosonic bath during the simulation time τ, where we apply the drive tones with frequencies ω_1 and ω_2 (see Sec. II C). As can be seen in the pulse sequence depicted in Fig. 8(b), the laboratory frame qubit frequency is tuned to the lower cutoff frequency ω_0 of the bosonic bath. This also corresponds to zero frequency in the effective frame, given by the rotating frame frequency $\omega_1 = \omega_0$. After the simulation of time τ, we apply an optional $\pi/2$ rotation prior to qubit readout. This allows us to measure $\langle\hat{\sigma}_x\rangle$ of the qubit state. If no rotation is applied, we measure the qubit state along its quantization axis $\langle\hat{\sigma}_z\rangle$.

2. Bath initialization

Within the above formalism we are able to probe the relaxation of qubit excitations for both $\langle\hat{\sigma}_z\rangle$ and $\langle\hat{\sigma}_x\rangle$. For a direct

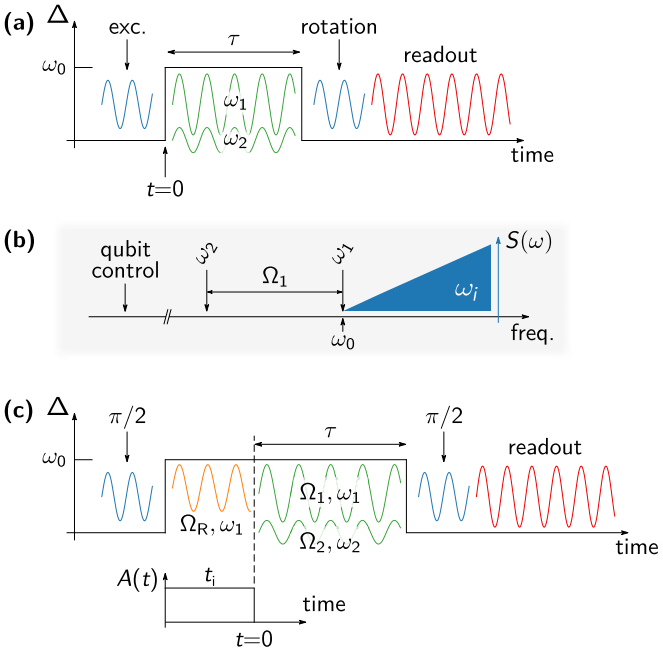

FIG. 8. Measurement protocols for the spin-boson simulator. (a) Pulse sequence for preparing an eigenstate of $\hat{\sigma}_z$ or $\hat{\sigma}_x$, with the qubit out of resonance with the bosonic bath, followed by interaction with the bath during time τ and readout. The qubit is tuned into the presence of the bosonic bath with a fast detuning pulse. Prior to dispersive qubit readout, we can rotate the qubit state in order to measure $\langle\hat{\sigma}_z\rangle$ or $\langle\hat{\sigma}_x\rangle$. (b) Schematic location of the drive frequencies ω_1 and ω_2. The spectral location of the bosonic bath with individual mode frequencies ω_i is schematically depicted in blue, indicating its spectral function $S(\omega)$. (c) Proposed pulse sequence for measuring $P(t)$ including a bath initialization scheme. The qubit is initially prepared in an eigenstate of $\hat{\sigma}_x$ via a $\pi/2$ rotation. At $t_i < t < 0$, we initialize the bosonic bath via a strong bath drive of amplitude Ω_R and frequency ω_1. For $t > 0$, we set $\Omega_R = 0$.

comparison with the spin-boson theory, for example, presented in Ref. [1], the environment has to be properly initialized in addition. On the other hand, a comparison between the results obtained using different initialization methods allows for experimentally exploring the effect of bath initialization in the spin-boson model.

In order to observe the well population function $P(t)$ as discussed in Ref. [1], the qubit in the spin-boson system is initially required to be in an eigenstate of $\hat{\sigma}_x$ for $t < 0$, with the bath being relaxed in thermal equilibrium within this condition. This can be achieved experimentally by applying a Rabi drive at the rotating frame frequency ω_1 of enhanced amplitude $\Omega_R = \Omega_1 + A(t)$. After the transformation in the interaction picture, this leaves an additional term in the effective spin-boson Hamiltonian

$$\hat{H}_{\rm eff} + A(t)\hat{\sigma}_x, \tag{86}$$

with $\hat{H}_{\rm eff}$ given in Eq. (23). Initialization is applied at an effective amplitude $A(t) = \Omega_R - \Omega_1 \gg g$, where g is the typical coupling strength between the qubit and the individual bosonic mode. Figure 8(c) shows a schematic of the proposed pulse sequence. Bath initialization takes place during $t_i < t < 0$, with t_i defined by the inverse spectral width of the bosonic bath. The simulation starts at $t = 0$, where the initialization drive is switched off, $A(t) = 0$, and the Rabi drives of the simulation scheme are switched on. To recover the well population function $P(t)$, we $\pi/2$ rotate the qubit state before readout in order to measure $\langle\hat{\sigma}_x\rangle$.

C. Bath heating

Dissipation of the bosonic bath can be implemented by adding an ancillary transmission line, providing a loss channel for bath excitations [72]. In our approach, dissipation takes place by Ohmic dissipation on chip and therefore involves Joule heating. The effect gives rise to a small modification of the bath spectral function. The main source of on-chip dissipation can be assumed to be the Rabi drive with amplitude Ω_1 and frequency ω_1, which in a realistic experiment also couples directly to the bath.

If we assume that the coupling between the drive and the bath is mediated by the qubit, the effective drive of the environment is of an approximate amplitude $(C_{ci}/C_{\rm int})\Omega_1$ per resonator i. Each resonator will couple to the drive with separate coupling. In the system considered in Sec. IV, each resonator has an approximative width $\gamma_i \lesssim 2\pi \times 5$ MHz. Considering explicitly the highest-energy resonator, with the off-resonance drive $\omega_i - \omega_1 \sim 2\pi \times 50$ MHz, we get an average photon number in this resonator

$$\langle\hat{n}_i\rangle \approx \left(\frac{C_{ci}}{C_{\rm int}}\right)^2\left(\frac{\Omega_1}{\omega_i - \omega_1}\right)^2 \lesssim 10^{-2}. \tag{87}$$

This leads to a photon dissipation rate $\Gamma_{\rm dis} = \gamma_i\langle\hat{n}_i\rangle \lesssim 1$ MHz. Due to the specific form of the designed impedance, the result is approximately the same for all individual resonators. The length of the one measurement process is roughly 1 μs, which implies that during one measurement each on-chip resistor absorbs on average less than one photon. The effect of this on the temperature of each resistor is small, but can set a minimal (cooling) time interval between two successive measurement protocols. Specific pulsing schemes that relax the environmental resonators to their ground states just before the quantum simulation can also be used [73–75].

VI. CONCLUSION AND DISCUSSION

We have shown that a quantum simulation of the spin-boson model can be performed in a wide parameter range using a superconducting qubit connected to a microwave circuit. In order to probe numerically difficult parameter regimes, we considered an extension of the driving scheme proposed in Ref. [18]. This effectively down-converts the system dynamics from the gigahertz to the megahertz regime, while preserving the order of the coupling strength between the two-level system and the environment. The approach allows for the observation of a quantum phase transition in a regime of a large effective Kondo parameter $\alpha \sim 1$, also without the use of a high-anharmonicity superconducting qubit. We find that this requires strong coupling between the qubit and microwave resonators in the laboratory frame. The phase transition region in the spin-boson model corresponds to a regime with an energy decay rate of the two-level system that is comparable to its effective transition frequency.

We discussed how to experimentally probe the well population dynamics $P(t)$ under different initialization conditions of the bosonic bath. For this purpose we provided concrete measurement pulse sequences, based on well-established control and detection schemes from circuit QED. In the system considered, probing the well population dynamics corresponds to measuring the expectation value of the $\hat{\sigma}_x(t)$ operator. It is also straightforward to study other two-level system correlation functions, such as of the $\hat{\sigma}_z(t)$ operator, as well as the effect of bath initialization.

The proposed approach allows for engineering a rather arbitrary spectral function in a restricted frequency range. We estimated that for a realization with a transmon qubit the spectral width of the environment must be in the range of 100 MHz. By controlling the drive and qubit frequencies, we can adjust the zero-frequency condition of the tailored bosonic bath, which allows us to choose the effective system temperature T_{eff}. By controlling the amplitude of the weaker Rabi drive Ω_2, we can tune the effective two-level system energy relative to the temperature and the cutoff frequency ω_c, which is of central importance in the spin-boson theory. In particular, Kondo physics can be observed for an effective temperature below the Kondo temperature T_K. At the Toulouse point ($\alpha = 1/2$) one can estimate [7] $k_B T_K \sim \hbar\Omega_2^2/\omega_c$, which can be adjusted by Ω_2. Hence, our system can access a large parameter space of the spin-boson model via experimental drive control. The proposed experimental approach, based on the flip-chip technique, also features a modularity that allows one to probe various fabricated bosonic environments with the same qubit in successive experiments.

ACKNOWLEDGMENTS

This work was supported by the European Research Council within consolidator Grant No. 648011 and Helmholtz IVF grant "Scalable solid state quantum computing". This work was also partially supported by the Ministry of Education and Science of Russian Federation in the framework of Increase Competitiveness Program of the NUST MISIS (Contracts No. K2-2014-025, No. K2-2016-051, and No. K2-2016-063). J.B. acknowledges financial support from the Landesgraduiertenförderung of the federal state Baden-Württemberg and by the Helmholtz International Research School for Teratronics.

APPENDIX A: DERIVING SPIN-BOSON MODEL PARAMETERS USING AN OPEN-CIRCUIT METHOD

In this Appendix we introduce the open-circuit method which can be used to model the considered dissipative circuits by treating the on-chip resonators by equivalent open transmission lines. For simplicity, we consider here the model of a Josephson junction coupled to a single dissipative LCR circuit, as shown in Fig. 9. The generalization to many resonators is straightforward but technically more involved than if determining the effective impedance classically, as done in the main text. Working with such explicit circuits helps one to check the validity of results based on more phenomenological approaches.

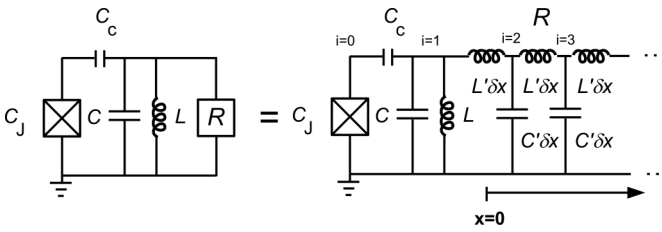

FIG. 9. Open-circuit model of a Josephson junction capacitively coupled to dissipative LC resonator.

1. Lagrangian

We consider a Josephson junction coupled to one dissipative resonator, as shown in Fig. 9. By representing the resistor as a semi-infinite transmission line, the total Lagrangian can be written as

$$\mathcal{L} = \mathcal{L}_{\text{env}} + \mathcal{L}_{\text{int}} + \mathcal{L}_{JJ}, \tag{A1}$$

where the environmental part corresponds to the Lagrangian of a semi-infinite transmission line

$$\mathcal{L}_{\text{env}} = \frac{C\dot{\Phi}_1^2}{2} - \frac{\Phi_1^2}{2L} + \sum_{i\geqslant 2}^{\infty} \frac{\delta x C'\dot{\Phi}_i^2}{2} - \sum_{i\geqslant 2}^{\infty} \frac{(\Phi_i - \Phi_{i-1})^2}{2L'\delta x}. \tag{A2}$$

The variable $\Phi_i(t)$ corresponds to the magnetic flux at node i and $\dot{\Phi}_i$ is the corresponding voltage. The interaction part reads

$$\mathcal{L}_{\text{int}} = \frac{C_c(\dot{\Phi}_1 - \dot{\Phi}_0)^2}{2} \tag{A3}$$

and the Josephson-junction part

$$\mathcal{L}_{JJ} = E_J \cos\left(\frac{\Phi_0}{\hbar/2e}\right) + \frac{C_J\dot{\Phi}_0^2}{2}. \tag{A4}$$

2. Hamiltonian

Derivation of the Hamiltonian starts from the identification of the conjugated variables of the fluxes. These are defined as $Q_i = \partial\mathcal{L}/\partial\dot{\Phi}_i$. We get

$$Q_0 = C_c(\dot{\Phi}_0 - \dot{\Phi}_1) + C_J\dot{\Phi}_0, \tag{A5}$$

$$Q_1 = C_c(\dot{\Phi}_1 - \dot{\Phi}_0) + C\dot{\Phi}_1, \tag{A6}$$

$$Q_{i\geqslant 2} = \delta x C'\dot{\Phi}_i. \tag{A7}$$

The inverse transformation has the form

$$\dot{\Phi}_{i\geqslant 2} = \frac{P_i}{\delta x C'}, \tag{A8}$$

$$\dot{\Phi}_1 = Q_1\frac{C_c + C_J}{C(C_c + C_J) + C_cC_J} + Q_0\frac{C_c}{C(C_c + C_J) + C_cC_J} \equiv Q_1\frac{1 + C_J/C_c}{\tilde{C}} + \frac{Q_0}{\tilde{C}}, \tag{A9}$$

$$\dot{\Phi}_0 = Q_0\frac{C_c + C}{C_J(C_c + C) + C_cC} + Q_1\frac{C_c}{C_J(C_c + C) + C_cC} \equiv Q_0\frac{1 + C/C_c}{\tilde{C}} + \frac{Q_1}{\tilde{C}}. \tag{A10}$$

Our Lagrangian corresponds to the Hamiltonian

$$H = H_{\rm env} + H_{\rm int} + H_{JJ}, \tag{A11}$$

where

$$H_{\rm env} = \frac{\Phi_1^2}{2L} + \frac{Q_1^2}{2(C+C_{p1})} + \sum_{i\geqslant 2}\frac{Q_i^2}{2\delta x C'} + \sum_{i\geqslant 2}\frac{(\Phi_i-\Phi_{i-1})^2}{2L'\delta x}. \tag{A12}$$

Here we have defined the series capacitance as seen by the resonator, $1/C_{p1} \equiv 1/C_c + 1/C_J$. If we identify $C_c = C_g$ (as in the main text) we have $C_{p1} = C_{\rm int}$. As the Lagrangian and Hamiltonian terms for Q_0 are the same as for Q_1, within the swap $C_J \leftrightarrow C_1$, we must have

$$H_{JJ} = -E_J\cos\left(\frac{2e}{\hbar}\Phi_0\right) + \frac{Q_0^2}{2(C_J+C_{p0})}, \tag{A13}$$

where analogously $1/C_{p0} \equiv 1/C_c + 1/C$. The junction and resonator capacitances are now renormalized as expected. The interaction term gets the form

$$H_{\rm int} = \frac{Q_0 Q_1}{\tilde{C}}, \quad \tilde{C} = C_J + C + \frac{C_J C}{C_c}. \tag{A14}$$

We note that in the main text the operator $\hat{Q}_0$ is marked simply $\hat{Q}$.

3. Solution

We have now determined the form of the Hamiltonian corresponding to the circuit of Fig. 9. The next step is to establish the solution when the interaction term is turned off. In the transmission line one obtains a wave equation whose solution can be written in the form

$$\hat{\Phi}(x>0,t) = \sqrt{\frac{\hbar R}{4\pi}}\int_0^\infty \frac{d\omega}{\sqrt{\omega}}[\hat{b}_{\rm in}(\omega)e^{i(-k_\omega x-\omega t)} + \hat{b}_{\rm out}(\omega)e^{i(k_\omega x-\omega t)} + {\rm H.c.}]. \tag{A15}$$

Here the characteristic impedance $R = \sqrt{L'/C'}$ and the wave number $k_\omega = \omega\sqrt{L'C'}$. The bosonic terms $\hat{b}_{\rm in}^\dagger(\omega)$ and $\hat{b}_{\rm in}(\omega)$ correspond to incoming photon-field creation and annihilation operators. They (as well as the out-field operators) satisfy $[\hat{b}_{\rm in}(\omega),\hat{b}_{\rm in}^\dagger(\omega')] = \delta(\omega-\omega')$.

The Heisenberg equations of motion at $i=1$ read

$$\dot{\hat{\Phi}}_1(t) = \frac{\hat{Q}_1}{C+C_{p1}} + \mathbf{0}\times\frac{\hat{\mathbf{Q}}_0}{\tilde{C}}, \tag{A16}$$

$$\dot{\hat{Q}}_1(t) = -\frac{\hat{\Phi}_1}{L} + \frac{\hat{\Phi}_2-\hat{\Phi}_1}{\delta x L'} \to -\frac{\hat{\Phi}_1}{L} + \frac{1}{L'}\frac{\partial\hat{\Phi}(x=0,t)}{\partial x}. \tag{A17}$$

In Eq. (A16) we have set the interaction term (boldface) to zero. The junction is now decoupled from the dissipative resonator. These equations lead to the relation

$$(C+C_{p1})\dot{\hat{\Phi}}(x=0,t) = -\frac{\hat{\Phi}(x=0,t)}{L} + \frac{1}{L'}\frac{\partial\hat{\Phi}(x=0,t)}{\partial x}. \tag{A18}$$

This is a boundary condition between the incoming and outgoing fields. The solution is obtained by Fourier transforming, which gives

$$\omega^2(C+C_{p1})[\hat{b}_{\rm in}(\omega)+\hat{b}_{\rm out}(\omega)] = \frac{1}{L}[\hat{b}_{\rm in}(\omega)+\hat{b}_{\rm out}(\omega)] + i\frac{\omega}{R}[\hat{b}_{\rm in}(\omega)-\hat{b}_{\rm out}(\omega)]. \tag{A19}$$

The solution is

$$\hat{b}_{\rm out}(\omega) = -\frac{1+i\frac{L\omega/R}{1-(\omega/\omega_1)^2}}{1-i\frac{L\omega/R}{1-(\omega/\omega_1)^2}}\hat{b}_{\rm in}(\omega). \tag{A20}$$

We find that at zero as well as at infinite frequency, the boundary condition gives $\hat{a}_{\rm out}+\hat{a}_{\rm in}=0$. Similarly, we find

$$\hat{b}_{\rm in}(\omega)+\hat{b}_{\rm out}(\omega) = -2i\frac{L\omega/R}{1-(\omega/\omega_1)^2 - iL\omega/R}\hat{b}_{\rm in}(\omega) \equiv A(\omega)\hat{b}_{\rm in}(\omega). \tag{A21}$$

This is proportional to the impedance of the parallel LCR circuit

$$Z_{\rm eff}(\omega) = \frac{1}{\frac{1}{R}+\frac{1}{i\omega L}+i\omega(C+C_{p1})} = \frac{R}{2}A^*(\omega), \tag{A22}$$

$${\rm Re}[Z_{\rm eff}(\omega)] = \frac{R}{4}|A(\omega)|^2. \tag{A23}$$

The solution for the interaction voltage has the form

$$V_{\rm int}(t) \equiv \frac{\hat{Q}_1(t)}{\tilde{C}} = -i\frac{C_c}{C_c+C_J}\sqrt{\frac{\hbar R}{4\pi}}\int_0^\infty d\omega\sqrt{\omega}A(\omega)\hat{b}_{\rm in}(\omega)e^{-i\omega t} + {\rm H.c.}, \tag{A24}$$

$$\langle V_{\rm int}(t)V_{\rm int}(0)\rangle_{T=0} = \left(\frac{C_c}{C_c+C_J}\right)^2\frac{\hbar}{\pi} \times\int_0^\infty d\omega\,\omega\,{\rm Re}[Z_{\rm eff}(\omega)]e^{-i\omega t}. \tag{A25}$$

This agrees with the results given in the main text.

APPENDIX B: SINGLE-MODE VERSUS CONTINUOUS-MODE TREATMENT OF A MICROWAVE RESONATOR

In this Appendix we study the connection between single- and continuous-mode treatments of a microwave resonator. In the preceding Appendix we already derived an example of the connection between single-mode and multimode treatments, by deriving an exact form of the amplitude function $g_i \propto A(\omega)$ in the case of a transmon coupled to a single dissipative LCR resonator [Eqs. (A22)–(A25)]. In this Appendix we consider relations between the single- and continuous-mode treatments by using the representation in (numerable) bosonic operators $\hat{b}_i$.

For simplicity, we consider here the case $q_0 = 2e$ (Cooper-pair box), generalization to other cases is straightforward. In the single-mode analysis, the relative coupling strength between the qubit and a mode of frequency ω_r (divided by the mode frequency) is given (in the absence of coupling capacitor) by

$$g = \sqrt{\frac{\pi Z_{LC}}{R_Q}}, \tag{B1}$$

where Z_{LC} is the characteristic impedance of a microwave resonator. On the other hand, for the continuous-mode description of the same broadened mode, it is the area of the peak that matters,

$$\frac{q_0^2}{2\pi\hbar}\int d\omega\, J(\omega) = \frac{1}{R_Q}\sum_i g_i^2 = \omega_r^2\frac{g^2}{2}, \tag{B2}$$

where we have used the information that in the case considered the integration over $J(\omega)$ is proportional to the characteristic impedance Z_{LC}. Here the values g_i^2 form a peak around the central frequency ω_r, describing a broadened resonator. We then obtain a connection between the single-mode and the continuous-mode treatments of the same peak in the spectral density

$$g^2 = \frac{2}{R_Q}\sum_i\left(\frac{g_i}{\omega_r}\right)^2 = \frac{1}{\pi\hbar}\sum_i\left(\frac{q_0 g_i}{\omega_r}\right)^2. \tag{B3}$$

We see that the (squared) total effective strength is proportional to the sum of the squared strengths of individual modes. Note also that in comparison to couplings g_i, the coupling g is normalized by ω_r, which means that it depends only on the characteristic impedance of the resonator [see Eq. (B1)].

We could also interpret such a single-mode peak as a single slice of an Ohmic spectrum, at frequency ω_r, with width $d\omega$ and total coupling g. This interpretation gives a relation

$$\frac{q_0^2}{2\pi\hbar}\int d\omega J(\omega) = \omega_r^2\frac{g^2}{2} = \alpha\omega_r d\omega. \tag{B4}$$

This leads to the identification

$$\alpha = \frac{1}{2}\frac{\omega_r}{d\omega}g^2. \tag{B5}$$

The variable $d\omega$ is so far arbitrary and stands here for the width of the chosen slice of the Ohmic spectrum. Also the variable g is not fixed.

If we decide to fix the frequency-normalized coupling g (not $\omega_r g$), i.e., keep the characteristic impedances independent of the frequency of the chosen slice, then the frequency interval between resonators $d\omega$ has to decrease with the position ω_r. This can be interpreted as the quality factors of individual resonators needing to be identical: The resonators are equivalent up to a frequency conversion. On the other hand, if we decide to fix $d\omega$, we obtain that the coupling needs to behave as $g^2 \propto \alpha d\omega/\omega_r$. This increases when decreasing ω_r. However, equivalently, the unnormalized couplings should behave as $(\omega_r g)^2 \sim g_i^2 \sim \alpha\omega_r d\omega$. This then shows that the actual (squared) couplings g_i^2 need to increase linearly with frequency, as expected.

It should be noted that when constructing an effective bath at high frequencies instead, the contributions of individual resonator frequencies ω_i in the effective couplings $\omega_i g$ can be treated as a constant. The bath can then be constructed by varying the resonator density or by manipulating couplings g by additional coupling capacitors, as described in the main text.

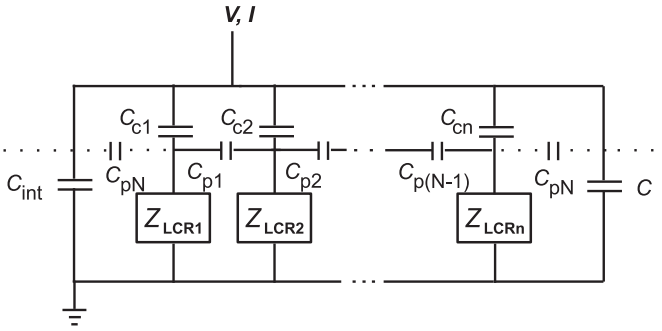

FIG. 10. Lumped-element model of the resonator bath with additional parasitic couplings C_{pi}.

APPENDIX C: DETERMINING THE IMPEDANCE OF THE ENVIRONMENT

We consider the generalized circuit shown in Fig. 10. We mark the voltage of island i, which is located between the capacitor C_{ci} and $LCRi$ element, by V_i. The impedance can then be evaluated from the conditions for the current conservation

$$\begin{aligned}
\frac{V-V_1}{Z_{C1}} &= \frac{V_1}{Z_{LCR1}} + \frac{V_1-V_2}{Z_{P1}} + \frac{V_1-V_N}{Z_{PN}},\\
\frac{V-V_2}{Z_{C2}} &= \frac{V_2}{Z_{LCR2}} + \frac{V_2-V_3}{Z_{P2}} + \frac{V_2-V_1}{Z_{P1}},\\
&\vdots\\
\frac{V-V_N}{Z_{CN}} &= \frac{V_N}{Z_{LCRN}} + \frac{V_N-V_1}{Z_{PN}} + \frac{V_N-V_{N-1}}{Z_{P(N-1)}}.
\end{aligned} \tag{C1}$$

Here we represent each circuit element by their equivalent impedance, for the coupling capacitor i this being $Z_{Ci} = (i\omega C_{ci})^{-1}$, for the parasitic coupling $Z_{pi} = (i\omega C_{pi})^{-1}$, and for the LCR element $Z_{LCRi} = (i\omega C_i + 1/i\omega L_i + 1/R_i)^{-1}$. The above set of equations can be represented as the matrix equation for island voltages V_i,

$$\begin{pmatrix} V/Z_{C1}\\ V/Z_{C2}\\ \cdots\\ V/Z_{CN}\end{pmatrix} = \begin{pmatrix} \frac{1}{Z_{C1}}+\frac{1}{Z_{LCR1}}+\frac{1}{Z_{P1}}+\frac{1}{Z_{PN}} & -\frac{1}{Z_{P1}} & \cdots & -\frac{1}{Z_{PN}}\\ -\frac{1}{Z_{P1}} & \frac{1}{Z_{C2}}+\frac{1}{Z_{LCR2}}+\frac{1}{Z_{P2}}+\frac{1}{Z_{P1}} & -\frac{1}{Z_{P2}} & \cdots\\ \cdots & \cdots & \cdots & \cdots\\ -\frac{1}{Z_{PN}} & \cdots & -\frac{1}{Z_{P(N-1)}} & \frac{1}{Z_{CN}}+\frac{1}{Z_{LCRN}}+\frac{1}{Z_{PN}}+\frac{1}{Z_{P(N-1)}}\end{pmatrix}\begin{pmatrix} V_1\\ V_2\\ \cdots\\ V_N\end{pmatrix}. \tag{C2}$$

The relative voltages V_i/V can then be straightforwardly solved numerically using matrix inversion. The impedance Z is solved using the relation

$$I = \sum_i \frac{V - V_i}{Z_{Ci}}, \tag{C3}$$

which then leads to the equation for impedance Z,

$$\frac{1}{Z} \equiv \frac{I}{V} = \sum_i \left[\frac{1}{Z_{Ci}} - \frac{1}{V} \frac{V_i}{Z_{Ci}} \right]. \tag{C4}$$

As discussed in the main text, the total effective impedance as seen by the qubit includes also capacitors C and $C_{\rm int}$. The answer for the total effective impedance is then

$$Z_{\rm eff} = (i\omega C + i\omega C_{\rm int} + Z^{-1})^{-1}. \tag{C5}$$

[1] A. Leggett, S. Chakravarty, A. Dorsey, M. Fisher, A. Garg, and W. Zwerger, Rev. Mod. Phys. **59**, 1 (1987).

[2] U. Weiss, *Quantum Dissipative Systems*, 3rd ed. (World Scientific, Singapore, 2008).

[3] A. Shnirman, Y. Makhlin, and G. Schön, Phys. Scr. **T102**, 147 (2002).

[4] P. P. Orth, A. Imambekov, and K. Le Hur, Phys. Rev. B **87**, 014305 (2013).

[5] M. Marthaler and J. Leppäkangas, Phys. Rev. B **94**, 144301 (2016).

[6] K. Le Hur, Phys. Rev. B **85**, 140506 (2012).

[7] M. Goldstein, M. H. Devoret, M. Houzet, and L. I. Glazman, Phys. Rev. Lett. **110**, 017002 (2013).

[8] F. B. Anders, R. Bulla, and M. Vojta, Phys. Rev. Lett. **98**, 210402 (2007).

[9] I. Georgescu, S. Ashhab, and F. Nori, Rev. Mod. Phys. **86**, 153 (2014).

[10] E. Manousakis, J. Low Temp. Phys. **126**, 1501 (2002).

[11] D. Porras, F. Marquardt, J. von Delft, and J. I. Cirac, Phys. Rev. A **78**, 010101(R) (2008).

[12] C. Schneider, D. Porras, and T. Schaetz, Rep. Prog. Phys. **75**, 024401 (2012).

[13] A. Lemmer, C. Cormick, D. Tamascelli, T. Schaetz, S. F. Huelga, and M. B. Plenio, arXiv:1704.00629.

[14] S. Mostame, P. Rebentrost, A. Eisfeld, A. J. Kerman, D. I. Tsomokos, and A. Aspuru-Guzik, New J. Phys. **14**, 105013 (2012).

[15] F. Mei, V. M. Stojanović, I. Siddiqi, and L. Tian, Phys. Rev. B **88**, 224502 (2013).

[16] J.-M. Reiner, M. Marthaler, J. Braumüller, M. Weides, and G. Schön, Phys. Rev. A **94**, 032338 (2016).

[17] L. García-Álvarez, J. Casanova, A. Mezzacapo, I. L. Egusquiza, L. Lamata, G. Romero, and E. Solano, Phys. Rev. Lett. **114**, 070502 (2015).

[18] D. Ballester, G. Romero, J. J. García-Ripoll, F. Deppe, and E. Solano, Phys. Rev. X **2**, 021007 (2012).

[19] J. Li, M. Silveri, K. Kumar, J.-M. Pirkkalainen, A. Vepsäläinen, W. Chien, J. Tuorila, M. Sillanpää, P. Hakonen, E. Thuneberg *et al.*, Nat. Commun. **4**, 1420 (2013).

[20] J. Braumüller, M. Marthaler, A. Schneider, A. Stehli, H. Rotzinger, M. Weides, and A. V. Ustinov, Nat. Commun. **8**, 779 (2017).

[21] M. Haeberlein, F. Deppe, A. Kurcz, J. Goetz, A. Baust, P. Eder, K. Fedorov, M. Fischer, E. P. Menzel, M. J. Schwarz *et al.*, arXiv:1506.09114.

[22] J. Clarke and F. K. Wilhelm, Nature (London) **453**, 1031 (2008).

[23] R. J. Schoelkopf and S. M. Girvin, Nature (London) **451**, 664 (2008).

[24] M. H. Devoret and R. J. Schoelkopf, Science **339**, 1169 (2013).

[25] J. Q. You and F. Nori, Nature (London) **474**, 589 (2011).

[26] X. Gu, A. F. Kockum, A. Miranowicz, Y. X. Liu, and F. Nori, Phys. Rep. **718-719**, 1 (2017).

[27] A. Blais, R.-S. Huang, A. Wallraff, S. M. Girvin, and R. J. Schoelkopf, Phys. Rev. A **69**, 062320 (2004).

[28] J. M. Fink, M. Göppl, M. Baur, R. Bianchetti, P. J. Leek, A. Blais, and A. Wallraff, Nature (London) **454**, 315 (2008).

[29] M. Hofheinz, H. Wang, M. Ansmann, R. C. Bialczak, E. Lucero, M. Neeley, A. D. O'Connell, D. Sank, J. Wenner, J. M. Martinis *et al.*, Nature (London) **459**, 546 (2009).

[30] G. Günter, A. A. Anappara, J. Hees, A. Sell, G. Biasiol, L. Sorba, S. De Liberato, C. Ciuti, A. Tredicucci, A. Leitenstorfer, and R. Huber, Nature (London) **458**, 178 (2009).

[31] A. A. Anappara, S. De Liberato, A. Tredicucci, C. Ciuti, G. Biasiol, L. Sorba, and F. Beltram, Phys. Rev. B **79**, 201303(R) (2009).

[32] J. Casanova, G. Romero, I. Lizuain, J. J. García-Ripoll, and E. Solano, Phys. Rev. Lett. **105**, 263603 (2010).

[33] P. Forn-Díaz, J. Lisenfeld, D. Marcos, J. J. García-Ripoll, E. Solano, C. J. P. M. Harmans, and J. E. Mooij, Phys. Rev. Lett. **105**, 237001 (2010).

[34] T. Niemczyk, F. Deppe, H. Huebl, E. P. Menzel, F. Hocke, M. J. Schwarz, J. J. Garcia-Ripoll, D. Zueco, T. Hümmer, E. Solano *et al.*, Nat. Phys. **6**, 772 (2010).

[35] A. Baust, E. Hoffmann, M. Haeberlein, M. J. Schwarz, P. Eder, J. Goetz, F. Wulschner, E. Xie, L. Zhong, F. Quijandría *et al.*, Phys. Rev. B **93**, 214501 (2016).

[36] F. Yoshihara, T. Fuse, S. Ashhab, K. Kakuyanagi, S. Saito, and K. Semba, Nat. Phys. **13**, 44 (2016).

[37] Z. Chen, Y. Wang, T. Li, L. Tian, Y. Qiu, K. Inomata, F. Yoshihara, S. Han, F. Nori, J. S. Tsai *et al.*, Phys. Rev. A **96**, 012325 (2017).

[38] S. J. Bosman, M. F. Gely, V. Singh, A. Bruno, D. Bothner, and G. A. Steele, Quantum Inf. **3**, 46 (2017).

[39] J. P. Martínez, S. Léger, N. Gheereart, R. Dassonneville, L. Planat, F. Foroughi, Y. Krupko, O. Buisson, C. Naud, W. Guichard *et al.*, arXiv:1802.00633.
[40] R. Gerritsma, G. Kirchmair, F. Zähringer, E. Solano, R. Blatt, and C. F. Roos, Nature (London) **463**, 68 (2010).
[41] M. Geiser, F. Castellano, G. Scalari, M. Beck, L. Nevou, and J. Faist, Phys. Rev. Lett. **108**, 106402 (2012).
[42] C. Maissen, G. Scalari, F. Valmorra, M. Beck, J. Faist, S. Cibella, R. Leoni, C. Reichl, C. Charpentier, and W. Wegscheider, Phys. Rev. B **90**, 205309 (2014).
[43] C. Ciuti, G. Bastard, and I. Carusotto, Phys. Rev. B **72**, 115303 (2005).
[44] M.-J. Hwang, R. Puebla, and M. B. Plenio, Phys. Rev. Lett. **115**, 180404 (2015).
[45] S. Ashhab and F. Nori, Phys. Rev. A **81**, 042311 (2010).
[46] J. Leppäkangas, M. Marthaler, D. Hazra, S. Jebari, R. Albert, F. Blanchet, G. Johansson, and M. Hofheinz, Phys. Rev. A **97**, 013855 (2018).
[47] A. F. Kockum, V. Macrí, L. Garziano, S. Savasta, and F. Nori, Sci. Rep. **7**, 5313 (2017).
[48] P. Forn-Díaz, J. García-Ripoll, B. Peropadre, J.-L. Orgiazzi, M. Yurtalan, R. Belyansky, C. Wilson, and A. Lupascu, Nat. Phys. **13**, 39 (2016).
[49] L. Magazzú, P. Forn-Díaz, R. Belyansky, J.-L. Orgiazzi, M. A. Yurtalan, M. R. Otto, A. Lupascu, C. M. Wilson, and M. Grifoni, Nat. Commun. **9**, 1403 (2018).
[50] A. Mezzacapo, U. L. Heras, J. S. Pedernales, L. DiCarlo, E. Solano, and L. Lamata, Sci. Rep. **4**, 7482 (2017).
[51] N. K. Langford, R. Sagastizabal, M. Kounalakis, C. Dickel, A. Bruno, F. Luthi, D. J. Thoen, A. Endo, and L. DiCarlo, Nat. Commun. **8**, 1715 (2017).
[52] W. Qin, A. Miranowicz, P.-B. Li, X.-Y. Lü, J. Q. You, and F. Nori, Phys. Rev. Lett. **120**, 093601 (2018).
[53] C. Leroux, L. C. G. Govia, and A. A. Clerk, Phys. Rev. Lett. **120**, 093602 (2018).
[54] J. Koch, T. M. Yu, J. Gambetta, A. A. Houck, D. I. Schuster, J. Majer, A. Blais, M. H. Devoret, S. M. Girvin, and R. J. Schoelkopf, Phys. Rev. A **76**, 042319 (2007).
[55] G. Schön and A. D. Zaikin, Phys. Rep. **198**, 237 (1990).
[56] G.-L. Ingold and Y. V. Nazarov, *Single Charge Tunneling: Coulomb Blockade Phenomena in Nanostructures* (Plenum, New York, 1992).
[57] S. Dambach, B. Kubala, V. Gramich, and J. Ankerhold, Phys. Rev. B **92**, 054508 (2015).
[58] J. Leppäkangas, M. Fogelström, M. Marthaler, and G. Johansson, Phys. Rev. B **93**, 014506 (2016).
[59] G. Ithier, E. Collin, P. Joyez, P. J. Meeson, D. Vion, D. Esteve, F. Chiarello, A. Shnirman, Y. Makhlin, J. Schriefl *et al.*, Phys. Rev. B **72**, 134519 (2005).
[60] B. Yurke and J. S. Denker, Phys. Rev. A **29**, 1419 (1984).
[61] D. M. Pozar, *Microwave Engineering*, 2nd ed. (Wiley, New York, 1998).
[62] M. Wallquist, V. S. Shumeiko, and G. Wendin, Phys. Rev. B **74**, 224506 (2006).
[63] R. Loudon, *The Quantum Theory of Light* (Oxford University Press, New York, 2010).
[64] M. Malekakhlagh and H. E. Türeci, Phys. Rev. A **93**, 012120 (2016).
[65] A. Parra-Rodriguez, E. Rico, E. Solano, and I. L. Egusquiza, Quantum Sci. Technol. **3**, 024012 (2018).
[66] A. Shnirman and Y. Makhlin, J. Exp. Theor. Phys. Lett. **78**, 447 (2003).
[67] J. Leppäkangas and E. Thuneberg, Phys. Rev. B **78**, 144518 (2008).
[68] M. H. Devoret, in *Quantum Fluctuations in Electrical Circuits, Proceedings of the Les Houches Summer School of Theoretical Physics, LXIII, 1995*, edited by S. Reynaud, E. Giacobino, and J. Zinn-Justin (Elsevier, Amsterdam, 1995).
[69] Z. K. Minev, K. Serniak, I. M. Pop, Z. Leghtas, K. Sliwa, M. Hatridge, L. Frunzio, R. J. Schoelkopf, and M. H. Devoret, Phys. Rev. Appl. **5**, 044021 (2016).
[70] J. Braumüller, Ph.D. thesis, Physikalisches Institut, Karlsruhe Institute of Technology, 2018.
[71] J. Braumüller, M. Sandberg, M. R. Vissers, A. Schneider, S. Schlör, L. Grünhaupt, H. Rotzinger, M. Marthaler, A. Lukashenko, A. Dieter *et al.*, Appl. Phys. Lett. **108**, 032601 (2016).
[72] G. Rastelli and I. M. Pop, Phys. Rev. B **97**, 205429 (2018).
[73] C. C. Bultink, M. A. Rol, T. E. O'Brien, X. Fu, B. C. S. Dikken, C. Dickel, R. F. L. Vermeulen, J. C. de Sterke, A. Bruno, R. N. Schouten *et al.*, Phys. Rev. Appl. **6**, 034008 (2016).
[74] D. T. McClure, H. Paik, L. S. Bishop, M. Steffen, J. M. Chow, and J. M. Gambetta, Phys. Rev. Appl. **5**, 011001 (2016).
[75] S. Boutin, C. K. Andersen, J. Venkatraman, A. J. Ferris, and A. Blais, Phys. Rev. A **96**, 042315 (2017).